LA-UR-24-20158

Accepted Manuscript

Ultimate compressive strength and severe plastic deformation of equilibrated single-crystalline copper nanoparticles

Liang, Zhao Magar, Nishchal Thapa Koju, Raj Kiran Chesser, Ian Wallace Zimmerman, Jonathan Mishin, Yuri Rabkin, Eugen

Provided by the author(s) and the Los Alamos National Laboratory (2024-06-19).

To be published in: Acta Materialia

DOI to publisher's version: 10.1016/j.actamat.2024.120101

Permalink to record:

https://permalink.lanl.gov/object/view?what=info:lanl-repo/lareport/LA-UR-24-20158







Los Alamos National Laboratory, an affirmative action/equal opportunity employer, is operated by Triad National Security, LLC for the National Nuclear Security Administration of U.S. Department of Energy under contract 89233218CNA000001. By approving this article, the publisher recognizes that the U.S. Government retains nonexclusive, royalty-free license to publish or reproduce the published form of this contribution, or to allow others to do so, for U.S. Government purposes. Los Alamos National Laboratory requests that the publisher identify this article as work performed under the auspices of the U.S. Department of Energy. Los Alamos National Laboratory strongly supports academic freedom and a researcher's right to publish; as an institution, however, the Laboratory does not endorse the viewpoint of a publication or guarantee its technical correctness.

Ultimate compressive strength and severe plastic deformation of equilibrated single-crystalline copper nanoparticles

Zhao Liang, Nishchal Thapa Magar, Raj Kiran Koju, Ian Chesser, Jonathan Zimmerman, Yuri Mishin, Eugen Rabkin

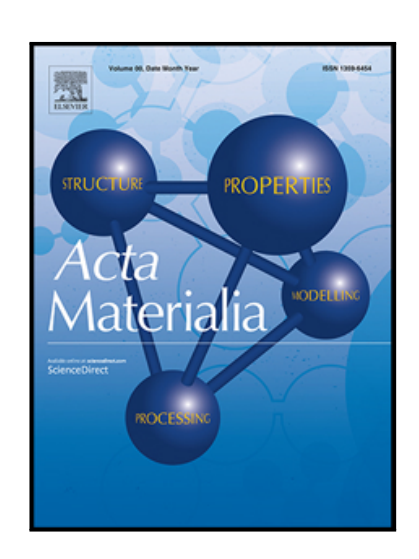
PII: \$1359-6454(24)00452-X

DOI: https://doi.org/10.1016/j.actamat.2024.120101

Reference: AM 120101

To appear in: Acta Materialia

Received date: 18 January 2024 Revised date: 30 May 2024 Accepted date: 10 June 2024



Please cite this article as: Zhao Liang, Nishchal Thapa Magar, Raj Kiran Koju, Ian Chesser, Jonathan Zimmerman, Yuri Mishin, Eugen Rabkin, Ultimate compressive strength and severe plastic deformation of equilibrated single-crystalline copper nanoparticles, *Acta Materialia* (2024), doi: https://doi.org/10.1016/j.actamat.2024.120101

This is a PDF file of an article that has undergone enhancements after acceptance, such as the addition of a cover page and metadata, and formatting for readability, but it is not yet the definitive version of record. This version will undergo additional copyediting, typesetting and review before it is published in its final form, but we are providing this version to give early visibility of the article. Please note that, during the production process, errors may be discovered which could affect the content, and all legal disclaimers that apply to the journal pertain.

© 2024 Published by Elsevier Ltd on behalf of Acta Materialia Inc.

Ultimate compressive strength and severe plastic deformation of equilibrated single-crystalline copper nanoparticles

Zhao Liang¹, Nishchal Thapa Magar², Raj Kiran Koju², Ian Chesser^{2,3}, Jonathan Zimmerman¹, Yuri Mishin², and Eugen Rabkin¹

May 30th, 2024

¹Department of Materials Science and Engineering, Technion-Israel Institute of Technology, 3200003 Haifa, Israel

²Department of Physics and Astronomy, MSN 3F3, George Mason University, Fairfax, VA 22030, USA

³Computational Physics Division, Los Alamos National Laboratory, Los Alamos, New Mexico 87545, USA

Abstract

Mechanical properties and deformation mechanisms of defect-free copper nanoparticles are investigated by combining experiments with atomistic simulations. The compressive strength of the particles increases with decreasing size and tends to saturate near the theoretical strength in the small-size limit. In this limit, the intrinsic size dependence of the strength is governed by the stochastic nature of dislocation nucleation near the particle surface. The particle deformation process evolves from the initial strain softening to strain hardening as the particle accumulates residual damage. The normalized strength-size relation for Cu is compared with those for Au, Ni, and Pt. The lack of universal behavior among the four FCC metals is discussed. Heavily deformed Cu nanoparticles develop polycrystalline structures and change the lattice orientation from [111] to [110]. The experiments and simulations reveal the twinning mechanism of the lattice rotation leading to the new grain formation.

Keywords: Nanoparticles, compressive deformation, dislocations, twinning.

1. Introduction

Plastic deformation of metallic objects smaller than a few micrometers in size has been extensively studied and is known to differ significantly from the plastic deformation of bulk metals and alloys [1]. A wealth of information has been obtained by micro-compression and micro-tension tests of metallic pillars with diameters ranging from a micrometer to hundreds of nanometers and machined with the aid of focused ion beam (FIB) instruments [2–5]. It has been demonstrated that the flow stress of such pillars is size-dependent and exceeds that of the respective bulk material by about an order of magnitude. Studies performed on FIB-machined pillars of several elemental face-centered cubic (FCC) metals revealed a universal power law relation between the flow stress normalized by an appropriate shear modulus and the pillar diameter normalized by the Burgers vector [6]. For Au, Cu, Ni, and Al pillars, the size exponent describing the increase in the pillar's strength with decreasing diameter was found to be n = 0.66, demonstrating universality of the underlying plasticity mechanisms.

The flow stress of the FIB-machined micro- and nanopillars is about an order of magnitude lower than the theoretical strength of the respective metals. The reason is that, despite their scarcity, pre-existing dislocations and their sources still dominate the plasticity. A GPa-level strength comparable to the theoretical strength could only be reached in single crystalline nanopillars, nanowires, and nanoparticles prepared by high-temperature methods such as directional solidification [7], molecular beam epitaxy [8,9], and solid-state dewetting [10–15]. The onset of plasticity in the defect-scarce nano-structures has been attributed to the stress required to initiate the dislocation nucleation. Compression testing of metallic micro- and nanoparticles by load-controlled nano-indentation revealed large elastic strains reaching 10% followed by an abrupt displacement burst and plastic collapse [10-15]. The latter was associated with massive nucleation of dislocations in the otherwise pristine particle. The nucleation of a new dislocation requires a much higher stress than the stress to move preexisting dislocations or activate existing dislocation sources [16]. Finding universal relationships in this nucleation-controlled plasticity is a difficult task because the deformation mechanisms depend not only on the specimen size [11–17] but also on its shape [14,18,19]. For example, the compressive strength of faceted Mo micro-particles exhibited a strong size effect, whereas the onset of plasticity in the rounded particles was found to be size-independent [13]. Moreover, at the stress level of several GPa, the non-linearity of the elastic properties of metals becomes significant, causing an asymmetry between the compressive and tensile behaviors [12].

Until now, nucleation-controlled compressive strength has been measured experimentally on faceted single-crystalline nanoparticles of the FCC metals Au [11,20], Ni [12], and Pt [14]. Out of them, Ni and Au have approximately the same normalized strength, while the normalized strength of Pt is about an order of magnitude lower. These results reveal a lack of universality in the nucleation-controlled plasticity of defect-free FCC nanoparticles. Several explanations have been proposed but no definitive conclusions could be reached based on the available experimental data. Further studies of faceted defect-free nanoparticles of other FCC metals are essential for understanding the plasticity laws in the nucleation-controlled regime.

The size exponents extracted from the micro-compression experiments on nanoparticles were found to be $n \approx 1.0$ for Pt [14] and $n \approx 0.8$ for Au [11] and Ni [12]. These exponents are

considerably higher than those observed in molecular dynamic (MD) simulations of particle compression, $n \approx 0.4 - 0.5$ [12,21]. The discrepancy between the experiments and simulations leads to a paradoxical situation: extrapolation of the experimental size dependence of strength to the particle sizes tested in the simulations gives a much higher strength than obtained by the simulations. In fact, the extrapolated strength is even higher than the theoretical strength of the material. It was suggested that this discrepancy is due to the larger probability of finding pre-existing dislocations and other defects in larger particles, leading to the overestimated size dependence of their strength [20]. Additional tests of a larger number of particles hinted at a possible saturation of the strength with decreasing size [14,20]. However, this trend could not be verified because of the insufficient statistics. It should be noted that the large scatter of the strength values is an intrinsic property of the stochastic nature of the nucleation-controlled process and is not related to instrumental errors [22,23].

Most previous micro- and nanoparticle compression studies were focused on the onset of plasticity defining the particle's strength. Less attention was paid to the severely deformed microstructure developed after the dislocation nucleation. This is understandable since, in most cases, the onset of plasticity is followed by a large and fast displacement burst, making the intermediate deformation stages experimentally inaccessible. Meanwhile, recent atomistic simulations of the compressive deformation of Ni-Co nanoparticles revealed interesting trends, such as the softening effect of alloying and solute-induced toughening of Ni-Co nanoparticles [24]. The particle toughness was related to the development of internal microstructure in the particles at intermediate plastic deformation stages.

This short overview motivates expanding the previous micro-compression studies of pristine metallic nanoparticles to include new FCC metals for understanding the general trends in nucleation-controlled plasticity. The present study focuses on FCC Cu nanoparticles. The stacking fault (SF) energy of Cu (40-50 mJ m⁻²) is close to that of Au (30-50 mJ m⁻²), lower than that of Ni (125 mJ m⁻²), and significantly lower than that of Pt (322 mJ m⁻²) [25]. Based on the SF energy criterion, the normalized strength of Cu particles is expected to be closer to that of Au and Ni particles than to the normalized strength of Pt particles. This hypothesis will be tested in this work. Also, we have tested significantly more particles than in any previous study. This enabled us to perform more accurate statistical analysis of the size dependence of the particle strength and compare the results with MD simulations. Since the previous study [14] indicated a strong impact of the particle shape on the compressive strength, we have carefully examined the particle shapes and only tested particles with shapes close to the equilibrium crystal shape (ECS) of Cu [26]. This allowed us to separate the size dependence from the particle shape effect. Furthermore, we employed the recently developed mass particle compression method [27] to access the intermediate stages of plastic deformation and directly compare the particle microstructures with those predicted by atomistic simulations. The extension of the previous work to another FCC metal, the access to a wider range of particle deformations, the significantly improved statistics, and the close integration with concurrent MD simulations have allowed us to gain new insights into the nanoscale deformation mechanisms in defect-free metallic objects.

To summarize this Section, the current work aims to explore the general trends in normalized shear strength among Ni, Au, Pt, and Cu nanoparticles and to test the hypothesis tying it to stacking fault energies. Further hypotheses are that the size effects on particle strength

determined in the experiment and in atomistic simulations should be consistent, and that postnucleation plastic deformation of nanoparticles is determined by the laws of dislocations nucleation, glide, and interaction in the nanoparticle.

2. Materials and Methods

2.1 Experimental methodology

The c-plane-oriented (0001) sapphire substrate was cleaned ultrasonically with acetone, isopropanol, ethanol, and de-ionized water prior to depositing a 30-nm-thick Cu film (99.999% purity) by electron beam evaporation. The as-deposited films were annealed under forming gas atmosphere (Ar-10% H₂, 99.99 vol.% purity) with a constant flow rate of 100 SCCM (Standard Cubic Centimeters per Minute) in a quartz tube furnace in the temperature range 900-1000°C and annealing times ranging from 12 to 72 hours. This heat treatment aimed to obtain equilibrated Cu nanoparticles with the ECS (Wulff-Kaischew shape).

Topographical images of the particles were obtained with a Park XE-70 atomic force microscope (AFM) operating in tapping mode and equipped with silicon probes with a radius of curvature of 10 nm at the apex. High-resolution AFM images of individual particles were obtained using the non-contact AFM mode (to avoid potential deformation of the particle surface) and an ultra-sharp tip with a nominal radius of curvature of 1 nm. The plan view morphology of the nanoparticles was characterized with a Carl Zeiss Ultra Plus High-resolution Scanning Electron Microscope (HR-SEM) using a secondary-electron detector and acceleration voltage of 3 keV. This characterization aimed to determine the top facet area and the projected area of the particle, which correlate with the contact area of indentation and the particle size, respectively.

The cross-sectional TEM specimen cut parallel to the {110} plane of a Cu particle was prepared using a dual beam FIB (FEI Helios Nanolab G3) and the standard "lift-out" method. The prepared TEM lamellae were examined using a mono-chromated and double aberration corrected field emission gun (scanning) transmission electron microscope (FEI Themis G2 80-300 keV S/TEM) to determine particles' microstructure and composition. The latter was visualized using elemental mapping in the scanning TEM (STEM) mode with an energy-dispersive X-ray spectroscopy (EDS) detector.

In-situ micro-compression tests of individual particles were performed with a Hysitron PI85 PicoIndenter working in displacement-controlled mode with a constant displacement rate of 1 nm s $^{-1}$ and equipped with a flat square diamond punch of 1 μ m in diameter. Only equilibrated particles were selected for the tests. They were placed beneath the diamond punch to align the loading direction of the punch with the particle surface normal. Only a single particle was compressed in each in-situ micro-compression test.

The deformation texture of the particles and the orientation relationship between the particles and the sapphire substrate were studied by automated electron backscatter diffraction (EBSD) mapping in a FEI Helios NanoLab G3 UC FIB DualBeam system equipped with EDAX Ametek Hikari XP2 EBSD detector. The EBSD scans were performed at the accelerating voltage of 30 keV with a 70° tilt.

The mass compression method introduced by Zimmerman and Rabkin [27] was employed to produce thousands of uniformly deformed Cu particles. In this method, the sapphire substrate with as-dewetted particles is covered with a clean piece of polished sapphire wafer, and the resulting "sandwich" is compressed using an Instron testing machine to produce a set of heavily deformed nanoparticles for further statistical analysis.

2.2 Simulation methodology

Interactions between Cu atoms were modeled using the well-tested embedded-atom method (EAM) potential that reproduces many experimental and first-principles data for this metal [28]. The MD simulations utilized the Large-scale Atomic/Molecular Massively Parallel Simulator (LAMMPS) [29]. The atomic structures were visualized and analyzed using the Open Visualization Tool (OVITO) [30]. The nanoparticles were initially created by the Wulff construction using the 0 K surface energies computed with the EAM potential. The initially sharp edges and corners of the particles were smoothed by the "simulated surface evaporation" procedure developed in [12]. The roundness parameter of 0.03 was chosen to best represent the experimental particle shapes. The particle size was defined as its effective diameter computed as the largest distance between the surface atoms in the directions parallel to the substrate. A set of 20 nanoparticles was created with diameters ranging from 17 nm to 90 nm. The number of atoms in the particles varied from 276,471 in the smallest nanoparticle to 39,428,515 in the largest.

The particles were subjected to simulated compression tests at the temperature of 300 K using a methodology similar to that used in the previous work [12,24]. In short, each particle was thermalized at 300 K and clamped between two virtual walls representing the substrate (lower wall) and the indenter (upper wall). Each wall was modeled by a harmonic force field with an effective elastic modulus of 100 GPa. The substrate position was fixed while the indenter was moved into the particle with a constant speed of 1 m s⁻¹. This process simulated the displacement-controlled particle deformation implemented in the experiments. The top and bottom facets of the particle had the (111) crystallographic orientation. The facet areas in contact with the walls were defined as nA₍₁₁₁₎, where n is the number of atoms on the facet, and A₍₁₁₁₎ = $a^2\sqrt{3}/4$ is the (111) surface area per atom (a being the FCC lattice constant). The engineering strain of the particle was computed by dividing the current displacement of the upper walls by the initial distance between the walls. The engineering compressive stress was obtained by F/A₀, where F is the total force exerted on the upper facet, and A₀ is the initial facet area.

The compressive strength of the particle was defined as the height of the first peak on the engineering stress-strain curve. The respective critical resolved shear stress (CRSS) was obtained by multiplying the peak stress by the Schmid factor for the four symmetrically equivalent {111} planes inclined relative to the top and bottom surfaces. The values of strength and CRSS reported below were obtained by averaging over five independent tests with different random velocity seeds. The error bars in the figures represent one standard deviation.

Several methods were applied to analyze the atomic structures, including visualization by the potential energy of atoms, the bond-angle analysis, and the dislocation extraction algorithm (DXA) implemented in OVITO. To calculate the dislocation density, the total length of all

dislocation types was computed using the Dislocation Analysis modifiers in OVITO. This length was divided by the particle volume obtained by multiplying the atomic volume of Cu by the number of atoms in the nanoparticle. To study the grain formation mechanisms under high compression, we applied the polyhedral template matching and grain segmentation algorithms from OVITO.

The inverse pole figures of the samples were generated by tracking the orientation matrix of the sample during the compression. The orientation matrix was determined through the orientation of the unit cell of the lattice (defined by the vectors connecting neighboring atoms) in the sample coordinate system [31]. The atoms belonging to different grains were identified and tracked using a parallel MPI code written for evaluating the orientation matrix.

3. Topic A: Compressive Strength of Equilibrated Cu Nanoparticles

3.1 Experimental results

Figure 1(a) shows the plan view morphology of Cu nanoparticles on the sapphire substrate obtained by solid-state dewetting at the temperature of 950°C for 48 hours (sample s3; see Section 1 of Supplementary Material for sample labeling). The equilibrium crystal shape (ECS) of Cu nanoparticles was achieved through a careful design of heat treatments (see Section 1 of Supplementary Material). The linear correlation between the height (determined with AFM) and the projected diameter (determined from plan view SEM micrographs) of the particles is an indication of self-similar equilibrium shape. The exact shape of an individual particle is well illustrated by AFM topography image in Fig. 2(a), with the out-of-plane (111) orientation and two prominent facet groups, {111} and {100}, which are confirmed by cross-sectional TEM micrograph in Fig. 2(b). Analyzing the shape of the particles with the aid of Winterbottom construction [32] yielded the value of 1.82 ± 0.15 J m⁻² for the Cu-Al₂O₃ interface energy, which agrees well with the value of 2.0 ± 0.1 J m⁻² reported by Curiotto et al. [33] (see Supplementary Material, Section 2). Only the particles with the ECS were selected for uniaxial micro-compression tests, with 144 nanoparticles tested in total. The SEM images of a typical particle before and after a micro-compression test are shown in Fig. 1(b) and (c), respectively. All load-displacement curves obtained exhibit a large elastic deformation followed by an abrupt strain burst (Fig. 3(a)). This burst is a signature of the dislocation nucleation-controlled plastic deformation. The onset of the strain burst corresponds to the nucleation of numerous new dislocations within the defect-free nanoparticle, resulting in a significant reduction in its strength. Since the particle can no longer support the load applied by the punch, it precipitously deforms into a pancake-like shape. The engineering stress in each individual particle at the onset of the strain burst was defined as the highest load divided by the top facet area obtained from the SEM micrograph. In what follows, this critical stress will be referred to as particle strength and denoted σ . The engineering strain was obtained by normalizing the punch displacement by the height of the pristine particle obtained from the AFM scan. The engineering stress-strain curves of nine selected particles in Fig. 3(b) show a size-dependent strength, with smaller particles exhibiting a higher strength.

The dependence of the particle strength σ on the projected diameter D is shown in Fig. 3(c). The projected diameters of the experimentally studied and simulated particles range from 178 to 757 nm, and from 17 to 90 nm, respectively. As the diameter decreases, the experimental

strength value increases from a minimum of 1.2 GPa to a maximum of 12.5 GPa. Notably, at sizes below 350 nm, the dependence of σ on D becomes weaker than for larger particles. Fitting all experimental results to the power-law equation $\sigma = AD^{-n}$, where A = const, yields the size exponent of $n = 1.0 \pm 0.1$. This value is comparable to those determined for defect-free nanoparticles in other FCC metals (0.8 to 1.0). However, even though the strength follows the "smaller is stronger" trend, there is a clear trend for the strength saturation for small particles. This is understandable since extrapolating the power law to small particle dimensions would yield strength values surpassing the theoretical strength limit. Previous studies also indicated a "plateau region" where the strength saturates [14,20,34] or even decreases with decreasing particle dimensions [35]. In the present work, due to the large number of self-similar Cu nanoparticles tested, it was possible to clearly identify two size dependence regimes of the particle strength. The turning point separating the two regimes corresponds to a diameter of 350 nm. The weak size dependence of the strength with D < 350 nm can be described by a power law with the size exponent of $n = 0.42 \pm 0.12$. The strength of larger particles is more sensitive to the size with the exponent of $n = 1.2 \pm 0.17$. Remarkably, the experimentally determined size exponent for the small particles is in excellent agreement with the MD simulations of the present work (size exponent of n = 0.39, see Section 3.2.1) as well as previous atomistic simulations [21].

3.2 Simulation results

3.2.1 The size dependence of particle strength

The goal of the atomistic simulations was to better understand the deformation mechanisms of the Cu nanoparticles. Figure 4 presents a typical nanoparticle shape evolution during the simulated compression tests. The initial shape (Fig. 4(a)) displays crystallographic facets with relatively smooth edges and corners. Some facets remain visible under a stronger compression, but most of the heavily deformed particles develop a rugged surface with multiple steps and slip traces (Fig. 4(b)). At the end of the compression test, the particle is compressed into a nearly flat, pancake-like shape (Fig. 4(c)) similar to the shape observed in the experiments.

Fig. 5(a) shows a typical stress-strain curve for a 40 nm nanoparticle. The deformation is initially elastic until the stress reaches about 15 GPa, at which point the particle undergoes the first yielding event and the stress abruptly drops to nearly zero. The deformation continues starting from an elastic mode, then the stress reaches another peak, and the process repeats. The first peak stress is the highest and thus represents the compressive strength of this particle. Fig. 5(b) summarizes the mechanical testing results. Each point represents an average of several tests performed on the same particle with different atomic velocity seeds. Note that the error bars of the individual points (not shown) are smaller than the point size. The main source of the statistical scatter of the points is related to the differences in the surface roughness of the particles caused by the stochastic nature of the smoothing process. Despite the statistical scatter, the results clearly show that the particle strength and CRSS increase with decreasing size, following the "smaller is stronger" trend.

Figure 6 presents a more detailed view of a typical stress-strain curve. Fig. 6(a) shows that the first peak of the stress is followed by a few more peaks of lower magnitude. This behavior represents a nanoscale strain softening effect, in which plastic deformation becomes easier once

the dislocation-free system undergoes the first yielding event. As deformation continues, the peaks become less regular and the average stress increases (Fig. 6(b)). Under further compression, the stress sharply increases and eventually reaches values higher than the first peak. The deformation enters the strain hardening regime in which the flow stress increases with plastic strain.

3.2.2 Dislocation mechanisms of nanoscale plasticity

MD snapshots were analyzed to understand the dislocation mechanisms of the nanoparticle deformation. At early stages of the deformation corresponding to the elastic portion of the stress-strain curve (Fig. 5(a)), multiple dislocation nucleation attempts were observed in which a small Shockley partial half-loop would form at the upper or lower facet but eventually recede. Such attempts continued until a critical nucleus formed that was capable of further growth into the particle. In most cases, the nucleus had the form of a leading partial with its ends attached to the surface (Fig. 7(a)). As it grew, a half-loop of the trailing partial nucleated at the surface, and the full dislocation obtained continued to glide across the particle with its ends attached to the surface. This first dislocation promoted the nucleation of other dislocations on the same or opposing facet, and soon multiple dislocations were gliding in different and often intersecting {111} planes. In some cases, homogeneous nucleation of a partial loop was observed under the top or bottom facet (Fig. 7(b)). The loop grew until it ran into a side facet, causing an avalanche of new nucleation events. In both cases, the dislocation nucleation and glide across the particle caused the first increment of the plastic strain, and the stress precipitously dropped to a small value. These observations confirm that the stress peak on the stress-strain curves is caused by the nucleation of the first dislocation on/near the particle surface. The dynamics of the dislocation network developing in a 35 nm particle during compression is shown in the Supplementary Movie M1.

The simulations also explain the dislocation mechanisms of strain softening and strain hardening of the nanoparticles. After the first burst of strain, most dislocations disappear by annihilation at the surface or with each other. The deformation continues in a nearly elastic regime. The stress increases until a peak value is reached at which a new dislocation avalanche occurs. The second peak is likely to be lower than the first because the surface steps and other defects created during the first avalanche facilitate the surface nucleation of new dislocations. In other words, the particle becomes softer. As the process repeats, more defects accumulate inside the particle in the form of dislocation debris and later sessile dislocation segments formed by cross-slip and intersection of dislocations gliding in nonparallel {111} planes. As the deformation continues, twins and later grain boundaries form in the particle. These defects restrain the motion of new dislocations, increasing the flow stress. Eventually, the deformation mode switches from nucleation-controlled to dislocation glide-controlled. The nanoparticle displays strain hardening similar to that in bulk materials.

The dislocation processes described above are quantified by the dislocation density plots shown in blue color in Fig. 6. At the initial stages of deformation, the stress peaks are accompanied by peaks of the dislocation density caused by the surges of dislocation activity. Between the stress peaks, the dislocation density reduces to nearly zero (Fig. 6(a)), confirming that the dislocations leave the particle recovering the initial defect-free state. As deformation continues,

the residual dislocation density between the peaks increases (Fig. 6(b)), reflecting the gradual accumulation of permanent damage that eventually leads to the strain hardening.

Note that the dislocation density measured in the deformed nanoparticles reaches extremely high values on the order of 0.02 nm⁻² rarely achievable in bulk materials. This high dislocation density is unique to nanoparticles. Even when a few dislocations are present in a 100 nm particle, they are separated by distances of tens of nm, which already accounts for the dislocation density shown in Fig. 6. Dislocation avalanches can temporarily create even higher dislocation densities.

3.3 Discussion

Our compression tests have revealed a significant size dependence of the nanoparticle strength with a relatively small scatter of the data points due to the self-similar equilibrated shapes of all particles. The large displacement bursts seen on the load-displacement curves (Fig. 3(a)) are caused by the onset of plasticity after accumulating a large elastic strain. This behavior confirms that the solid-state dewetting resulted in defect-free nanoparticles that can only be deformed plastically by the nucleation of new dislocations. The large number of tests with a relatively small statistical scatter has allowed us to identify two different regimes of the size dependence of strength. The particles larger than approximately 350 nm follow the power-law size dependence with the exponent of n = 1.2, while the particles smaller than 350 nm are characterized by a smaller size exponent of n = 0.42. The latter is in good agreement with MD simulations and represents the intrinsic behavior of truly defect-free nanoparticles. Their plastic deformation is triggered by dislocation nucleation in regions with the largest stress concentration, such as the edges and corners of the facets, as demonstrated in previous work [11,13] and the present MD simulations. We propose that the transition in the dependence of the particles' strength on their size at diameters of 350 nm occurs due to the changing location of dislocation nucleation events: Small particles (D<350nm) exhibit nucleation primarily at the free particle surface, while the dislocations in their larger counterparts (D>350nm) nucleate within the particle volume in the vicinity of pre-existing defects lowering the energy barrier for dislocation nucleation and weakening the particles. Since the probability of finding a defect in the particle increases with its size, this defect-assisted nucleation leads to a stronger size effect and increases the size effect exponent. As for the nature of these internal defects, glissile dislocations belonging to the octahedral slip system cannot represent such defects since they easily vanish at the initial stage of loading in a process known as "mechanical annealing" [36]. On the other hand, the presence of sessile dislocations has been documented in Au and Pt nanoparticles produced by solid-state dewetting [11,37]. While remaining immobile upon loading, such dislocations can lower the energy barrier for the nucleation of new dislocations through their long-range stress field.

Concerning the absolute value of the "intrinsic" size effect exponent of 0.42, the only explanation available in the literature relates this exponent to the scaling law of normal stress decay close to the edges of the particle's top facet [11,13,21]. The size exponent is close to 0.5 for the particles with sharp edges [11,21] and decreases to about 0.38 for the particles with highly rounded edges [13]. In this respect, this exponent is universal since it only depends on the particle's shape.

Interestingly, the intrinsic size exponent is lower than the value of n = 0.66 obtained for FIB-machined nano- and micro-pillars of elemental FCC metals [1,6]. This significant difference can be attributed to different deformation mechanisms. While the yielding of pristine metallic nanoparticles is controlled by dislocation nucleation, the current consensus is that the larger size effect observed in FIB-machined pillars is governed by the statistics of lattice defects and the size dependence of the stress required to activate isolated dislocation sources, such as pre-existing dislocations and FIB-induced surface damage, in FIB-milled samples.

To better understand the origin of the ultra-high strength of the defect-free particles, we have constructed an Ashby map of the CRSS normalized by the shear modulus G versus the particle diameter D normalized by Burgers vector b for the nanoparticles of four FCC metals fabricated by solid-state dewetting (Fig. 3(d)). This type of normalization yields a universal size dependence of the flow stress of FIB-machined pillars of several FCC metals. In the present study, the highest CRSS value obtained by multiplying the compressive strength by the Schmid factor of the (111) $\langle 112 \rangle$ partial dislocations is 4.1 GPa (G/10). All particles with normalized diameters below 1000 (equivalent to the actual diameter of 350 nm) fall within the theoretical shear strength region ranging from G/8 to G/30. This range closely aligns with the particle size region exhibiting the smaller power-law exponent. In contrast to the FIB-machined pillars, the Ashby plots for pristine nanoparticles of the four FCC metals do not follow a universal behavior. The plot for Pt is in the lower strength region, Ni and Au exhibit a higher normalized strength, and Cu falls in between. Several factors that could be responsible for the lack of universality in the chosen coordinates, including the following:

- It was suggested that the presence of a thin native oxide (or possibly hydroxide) layer on the surface of Ni particles contributes to their record-breaking strength [12]. However, the Cu particles studied here also form a native surface oxide layer of about 4 nm in thickness (Fig. 2(c)), yet they are weaker (in relative terms) than the Ni particles. At the same time, the Au particles do not form a native oxide but exhibit a normalized CRSS very close to that of Ni. Thus, the native oxide layer can be ruled out as the cause of the observed non-universal behavior.
- It was proposed that systematic variations in the particle shape are responsible for the observed differences in the strength [14]. However, the Cu particles tested in this work exhibit the ECS very close to that of Au [11]. Thus, the particle shapes cannot dominate the relative strength behavior displayed in Fig. 3(d).
- The differences in the stacking fault energies γ_{CTB} cannot explain the non-universal behavior Fig. 3(d) either. The γ_{CTB} values of the four metals rank in the order $\gamma_{CTB}(Pt) > \gamma_{CTB}(Ni) > \gamma_{CTB}(Cu) > \gamma_{CTB}(Au)$. The relative strength values in Fig. 3(d) do not follow this ranking. Namely, the relative strength increases in the order Pt-Cu-Au-Ni, with Ni exhibiting the highest relative strength instead of the expected placement between Pt and Cu.

Based on the available experimental data, we propose that the non-universality exemplified by Fig. 3(d) may originate from the normalization of strength using the linear shear modulus, which may be significantly modified under extreme compression stress characteristic of microcompression tests of pristine metal nanoparticles.

Conventionally, metals exhibit elastic behavior under low strains, where stress is linearly related to strain according to Hooke's law. However, at compressive stress levels reaching tens of GPa and ultrahigh strains exceeding 10%, the resistance of the material to shear in the plane normal to the applied compressive stress can significantly increase, which can be formally described in terms of the increase of the shear modulus. For example, in the simplest framework of the hard-ball model of a crystal, sliding two adjacent {111} layers past each other leads to a slight normal expansion of the crystal. Thus, the compressive stress applied normal to these planes should increase the crystal resistance to shear. Formally, this increase can be described in terms of increased shear modulus for small shear strains or in terms of increased energy of the unstable stacking fault for larger strains. We conjecture that the exact type of this dependence is material-specific and that normalizing the experimentally determined shear strength of the particles by appropriately selected stress-dependent shear modulus may help to establish some universality in the mechanical behavior of nanoparticles of FCC metals.

It is important to note that while the normalized strength of Pt appears to be the lowest among the four FCC metals, this does not necessarily imply that the non-linear elasticity effects in Pt are more pronounced than in other studied metals. Rather, the normalized strength of all four metals would be modified once the correct shear moduli are employed in the calculations. We emphasize the importance of determining correct elastic moduli (i.e. with the aid of atomistic simulations) for the future nanomechanical studies of pristine ultra-strong materials.

4. Topic B: Mass compression and microstructure of severely deformed Cu nanoparticles

4.1 Experimental results

4.1.1 Mass compression of Cu nanoparticles

A sapphire substrate of 3×3 mm² in size with attached dewetted nanoparticles was subjected to uniform compression with an Instron machine. Another polished and cleaned sapphire wafer was placed on top of the substrate, and a maximum load of 950 N was applied to it (Fig. 8(a)). The shape of the nanoparticles was examined by AFM before and after the compression. In contrast to the pico-indentation of individual particles, the mass compression results in a large number of homogeneously deformed particles with varying degrees of strain, enabling statistical analysis of the deformation texture. In Fig. 8(b), we plot the height h of the deformed particles against their as-dewetted diameter D for comparison with the undeformed particles. The aspect ratio h/D characterizes the particle shape while the height ratio h/h_0 (h_0 being the height of the as-dewetted particle) is a measure of the particle deformation. The plot shows that the particles larger than 400 nm and smaller than 200 nm have reached deformations up to 80% and 60%, respectively. The AFM topography images and SEM side views of the as-dewetted and deformed particles are illustrated in Fig. 8(c) and (d), respectively.

4.1.2 Microstructure of severely deformed Cu nanoparticles

The deformation texture of the nanoparticles was examined using EBSD in the dual-beam FIB. An area of $50 \mu m$ by $120 \mu m$ containing over 800 nanoparticles was scanned before and after the mass compression to analyze the statistically significant changes in the texture. The as-

dewetted nanoparticles displayed a predominant [111] out-of-plane orientation while maintaining two equivalent in-plane orientation relationships with the sapphire substrate due to twinning, $Cu(111)[1\bar{1}0] \parallel Al_2O_3(0001)[10\bar{1}0]$ and $Cu(111)[\bar{1}10] \parallel Al_2O_3(0001)[10\bar{1}0]$, as evidenced by the pole figures in Fig. 9(a) and (c). Following the mass compression, the texture of the deformed particles exhibited a clear tendency to rotate towards [110] from the original [111] out-of-plane orientation, as evidenced by the inverse pole figures in Fig. 9(a) and (b). The presence of a single peak at the center of the [110] pole figure of the deformed particles indicates that the rotation is complete, reaching the [110] endpoint for both directions corresponding to the two symmetric in-plane orientation relationships between the nanoparticles and the substrate. It was found that the deformed particles fell into two categories: (1) single crystals with a predominant [110] out-of-plane orientation and sub-grains at the particle edges (Fig. 9(d)), and (2) polycrystalline structures with high-angle grain boundaries (Fig. 9(e)). Most of the deformed particles were in the first category (Fig. 9(g)). Particles of the second category often contained grains with a [112] out-of-plane orientation. Such grains are the main contributors to the minor peak in the inverse pole figure of the deformed particles (Fig. 9(b)). A closer EBSD examination reveals detailed features of the two categories of particles. Category 1 particles consist of large deformed particles with an out-of-plane orientation of [110], depicted in green, and small, less deformed particles colored in blue (i.e. close to the initial [111] out-of-plane orientation), see Fig. 10(a). The presence of the latter particles is due to the "shadowing effect". This effect is attributed to the elastic deformation of the sapphire substrate and the compressing wafer by large particles (or dust contamination) during compression, resulting in shadow areas where nearby smaller particles undergo less deformation. Category 2 particles, which are severely deformed, display clear signs of deformation twining, characterized by two misoriented grains with [110] and [112] out-ofplane orientations. Remarkably, the in-plane orientation relationship remains unchanged, namely $[1\bar{1}0] \parallel [10\bar{1}0]$, as confirmed by the pole figures in Fig. 9(b) and (c). The misorientation line profiles of category 2 particles indicate a grain boundary misorientation angle close to 60 degrees (see Fig. 10(b)), confirming their twinned nature, which is consistent with the TEM results presented in Fig. 11.

We have carefully analyzed a selected group of particles before and after deformation for the relationship between the particle's degree of rotation and the compressive strain, as shown in Figure 10(c). Both categories show a linear relationship between the misorientation and strain, in the strain ranges of 20 to 80% and 40 to 65% for the particles of categories 1 and 2, respectively. The points corresponding to the single crystalline particles of category 1 are colored in green, while the points corresponding to bicrystalline particles of category 2 are colored in blue and red. The results qualitatively agree with the MD simulations presented in Fig. 10(d), indicating that the lattice rotation begins at the onset of plastic deformation.

To examine the structural changes caused by the deformation, a TEM lamella normal to the rotation axis $[1\bar{1}0]$ was prepared from a particle moderately deformed by the mass compression method. The annular dark field (ADF) micrograph in Fig. 11(a) shows that the deformation has transformed the single crystalline pristine particle into a polycrystalline one. Two grains are observed with out-of-plane orientations close to [110] and [112] for the upper and the lower grains, respectively. The grains are separated by a planar inclined grain boundary. The high-resolution STEM micrograph of the grain boundary reveals that its plane is parallel to the (111) crystallographic plane of the upper grain, suggesting that this grain boundary may be close to

a coherent twin boundary. As discussed below, this conjecture was confirmed by the atomistic simulations. Furthermore, a high magnification bright field micrograph of the particle's top surface reveals significant faceting caused by the compression. Clear (111) facets of approximately 10 nm in length are observed, separated by {111} slip steps on the surface. These facets correspond to the original top (111) facet of the undeformed particle rotated due to the deformation. The rotated (111) facets are parallel to the inclined grain boundary, again hinting at the possibility that the upper grain is in a twinning orientation relationship with the lower grain and that it was nucleated by twinning dislocations propagating along the (111) plane rather than one of the oblique {111} planes. This twinning mechanism is consistent with the MD simulations discussed below.

4.2 Simulation results

4.2.1 Severe plastic deformation and lattice rotation

At the end of the simulated compression tests, the particles were compressed into a pancake-like shape. In some cases, the particles developed a significant sidewise shear in a direction parallel to the substrate. The severe plastic deformation was typically accompanied by lattice rotation and often resulted in a polycrystalline structure. One example was presented in Fig. 12(a) for a 40 nm nanoparticle.

The mechanism of new grain formation was investigated in detail. It was found that, at early stages, the compression created deformation twins near either the top or the bottom facet, or both (Fig. 12(a)). Some of the twins eventually disappeared as a result of dynamic recrystallization (Fig. 12(b)). Instead, new grains (not necessarily twin type) nucleated at the periphery of the particle and grew towards its center (Fig. 12(c)). The dynamics of twin nucleation in a 40 nm particle is illustrated in the Supplementary Movie M2.

The twin formation has been confirmed as the mechanism of the particle reorientation from the [111] to the [110] axis discussed in section 4.1.2. The process is detailed in Fig. 13 using a fiduciary line to track the lattice rotation. After a certain degree of deformation, the particle starts tilting to the side as its [111] axis rotates towards one of the [100]-type directions. Such directions are symmetrically equivalent, and one of them is chosen randomly by a fluctuation. When the [112] axis becomes nearly parallel to the load direction, a twin nucleates near the top or bottom of the particle. In Fig. 13(a)-(d), two twins nucleate from the top and bottom. The twins grow and gradually consume much of the parent grain while their [110] direction rotates towards the normal to the substrate. These lattice rotations are confirmed by the inverse pole figures in Fig. 13(f) and (g). This process described here results in a two-grain structure containing the parent and a twin grain (or two twin grains), as was indeed observed in the experiments (Figs 10 and 11). The twin may consume the entire parent grain, resulting in a single crystalline particle with the [110] orientation. This was also found in the experiments. At later stages of compression, new non-twin grains can form near the periphery of the particle (Fig. 12(c)), producing a polycrystalline particle. The dynamics of twin-mediated rotation of a 40 nm particle is illustrated in the Supplementary Movie M3.

4.3 Discussion

Theoretically, compression of a (111)-oriented single crystal should retain the original crystal orientation since it activates all three {111} slip planes with two slip directions in each plane with equal probability, resulting in axial symmetry of the plastic flow. However, the current understanding based on earlier works [38] is that this mode of compression is unstable. Small fluctuations during the deformation lead to crystal rotation [39].

There are two possible paths for this rotation. If the initial deviation from the $\langle 111 \rangle$ axis increases the Schmid factor in one of the three {111} planes, then two slip directions can be activated in this plane. This slip results in rotation of the [110] direction towards the compression axis along the respective edge of the crystallographic triangle (Fig. 14(a)). As a consequence of the lattice rotation, the Schmid factor of the (111)[110] slip system corresponding to the (111) plane that was initially normal to the compression axis increases, eventually reaching that of the active slip system once the exact [110] crystal orientation is reached. The operation of these two {111} slip systems (with two slip directions in each plane) stabilizes the [110] crystal orientation upon further compression, and the rotation stops (Fig. 14(a)). Another possible scenario is when the spontaneous deviation from the original [111] axis creates an equal increase in the Schmid factor for two of the three {111} slip planes, in which only one slip direction can be active. In this case, the crystal rotates towards the [112] axis. It should be noted that in experiments on macroscopic single crystals, this simple picture is masked by intrinsic defects and insufficient statistics [40]. The mass particle compression implemented in this work enables an unprecedented statistical sampling of thousands of pristine single crystals with the exact (111) orientation of the compression axis.

Statistical analysis of the deformation texture obtained from the EBSD data on the deformed sample reveals crystal rotation from the [111] to the [110] normal orientation, a pattern similar to that observed in bulk single crystals. The pole figures of the deformed particles show that the initial out-of-plane orientation of (111) deviates from the central point in two directions corresponding to two twin-related in-plane orientations of the Cu particles. At the same time, the (110) plane rotates towards the center (Fig. 9(b)). The single peak in the (110) pole figure around the center confirms the completion of the rotation towards the [110] stable orientation for Cu particles with two in-plane orientations. The inverse pole figure presented in Fig. 9(b) demonstrates that most of the particles underwent rotation and eventually reached the final [110] orientation. A small minority arrives at the [112] orientation, indicating the duplex slip on two slip planes and a rotation path along the [111]-[001] line of the crystallographic triangle.

The linear relationship between the misorientation and strain observed in the experiment (Fig. 10(c)) is in good agreement with the results of MD simulations (Fig. 10(d)). However, there is a noticeable difference in slopes as the onset of [110] orientation occurs at around 80% strain in experiments and 65% strain in simulations. In simulations, the plastic strain translates into lattice rotation more efficiently than in experiments. This difference can be attributed to the ideal slip conditions and smaller particle sizes in the simulations, precluding complex dislocation reactions within the particles. While in our mass particle compression experiments the entire sample was severely deformed, hindering the capture of the early stage of deformation twinning, the experimental results successfully depict the later stage of twinning structures in the strain range from 40 to 65%. This closely aligns with simulation results, which

indicate the nucleation of twins at a strain of 28%. These findings highlight the agreement between experimental and simulation results and provide valuable insights into the deformation mechanisms of the investigated particles.

Moreover, Fig. 9(e) demonstrates a severely deformed particle with the co-existing [112]- and [110]-oriented grains, indicating recrystallization and formation of new grains separated by high-angle grain boundaries during the deformation. This mechanism of new grain formation in bulk samples is only possible during severe plastic deformation with plastic shear strains much larger than one [41]. As we will show below, the experiments indicate that the recrystallization in the nanoparticles proceeds via deformation twinning.

The TEM micrograph in Fig. 11 shows a deformed particle with two grains separated by a grain boundary. This particle falls under the second category of deformed particles mentioned in Section 4.1.2, with the grains oriented in the [110] and [112] out-of-plane directions (Fig. 9(e)). We propose that such polycrystalline particles form by deformation twinning. At the onset of plasticity, two oblique slip planes of the {111} family are activated, and the particle starts rotating towards the vector sum of these two slip planes, namely [100], as illustrated schematically in Fig. 14(b). At this stage, the Schmid factor for the leading Shockley partial is lower than for the trailing one [42]. As a result, the nucleated leading partial is swiftly followed by a trailing one, and the plastic deformation occurs via slip and interaction of dissociated full dislocations. As the rotation progresses and out-of-plane particle orientation moves closer to [100], the Schmid factor for the leading Shockley partial becomes larger than for the trailing one. The formation of a planar stacking fault extending into the particles becomes more likely because of the difficulty in nucleating a trailing partial. Nucleation of another leading partial (which can also be considered a twinning dislocation) on the neighboring {111} plane results in the formation of an embryonic twin (Fig. 14(b)). This twin continues to grow, eventually forming a new grain. Meanwhile, the parent grain continues to rotate toward the [100] orientation, eventually arriving at the stable [112] orientation. In the twinned grain, only one {111} slip plane is active, so this grain eventually arrives at the [110] out-of-plane orientation. Thus, it is highly likely that the polycrystalline particles shown in Fig. 9(e), Fig. 10(a) and Fig. 11 have formed by deformation twinning. We emphasize that deformation twinning at room temperature has never been observed in bulk Cu.

The proposed recrystallization mechanism is consistent with the observation that the defect-free twinned grain could be readily visualized by TEM (Fig. 11). At the same time, no TEM image could be obtained from the lower grain. The lower grain represents the severely deformed parent lattice with a high density of entangled dislocations preventing us from obtaining a clear TEM image. The proposed mechanism is also confirmed by the present MD simulations as illustrated in Fig. 13.

The dislocation activity in the particle during the compression results in a serrated top surface morphology resembling surface faceting (Fig. 11(c)) [43]. However, the physical mechanisms of surface faceting and the formation of serrated surface topography observed in this work are quite different. The surface faceting is driven by the reduction of the total energy of the surface with a prescribed average orientation. The facets are patches of atomically flat surfaces of particularly low energy (i.e., {111} and {100}), with neighboring facets contacting each other along sharp edges. The individual facets grow by capillarity-driven surface diffusion [44]. In

contrast, the serrated surface topography observed here is caused by an interplay between dislocation slip and pressure-driven atomic migration, resulting in the smoothed surface topography with rounded asperities (Fig. 11(c)). To show the difference between the classical surface faceting and the formation of surface serrations, we note that the linear dimensions of the surface facets L scale with time t according to the relation $L \approx (Bt)^{1/4}$, where B is Mullins' coefficient [44]:

$$B = \frac{D_s \delta \gamma_{pv} \Omega}{kT}$$

Here, D_s , δ , and Ω are the surface self-diffusion coefficient, the thickness of the surface layer with mobile atoms, and the atomic volume, respectively. kT has its usual thermodynamic meaning. Using the Arrhenius parameters from Bradshaw et al. [45], we estimate $D_s \approx 7.3 \times 10^{-22} \,\mathrm{m^2 \, s^{-1}}$ at room temperature. Calculations show that during the characteristic compression time of 10 min, the average facet width would be about 1 nm, an order of magnitude smaller than observed in our experiments (Fig. 11(c)). This discrepancy demonstrates that the formation mechanism of the surface serrations cannot rely on capillary-driven surface self-diffusion alone. We also note that the rounded surface asperities increase the number of active surface sites, which may be of interest in functional applications of the particles.

It should be noted that the deformation behavior of a particle attached to a rigid substrate can be different from that of a bulk single crystal. The substrate can play a significant role in the loss of the initial slip symmetry of the [111]-oriented nanoparticles. For example, the Cu particles studied here predominantly rotated along the $[1\bar{1}0]$ axis and not the other two axes, $[10\bar{1}]$ and $[01\bar{1}]$, which are symmetrically equivalent. We relate this preference for the rotation axis to the mis-cut of the sapphire substrate (Fig. 14). The mis-cut direction was determined by aligning the pole figure of the deformed particles with the pole figure of the sapphire substrate. In the pole figure of the deformed particles, a slight deviation from the center was observed in the direction of $[11\bar{2}0]Al_2O_3$, indicating that the mis-cut direction is perpendicular to both $[11\bar{2}0]Al_2O_3$ and $[1\bar{1}0]Cu$. This observation suggests that the mis-cut direction of the sapphire substrate is the leading factor in breaking the symmetry at the onset of plasticity. Once the symmetry is broken, most of the particles rotate towards the stable [110] orientation, similar to their bulk single crystalline counterparts. However, contrary to the bulk crystals, in the nanoparticles this rotation can be accomplished by either dislocations glide on the active slip systems or a combination of glide with deformation twinning leading to recrystallization.

To summarize Section 4.3, we have elucidated two main rotation mechanisms of the nanoparticles of FCC metals during compressive deformation. One mechanism, slip-controlled rotation from [111] to [110], mirrors that of bulk materials, while the other involves deformation twinning at [112] orientation leading to the same final [110] orientation. The good agreement between experimental observations and atomistic simulation results contributes to a deeper understanding of the post-nucleation particle plasticity and crystal lattice rotation mechanisms.

5. Conclusions

- 1. We applied the solid-state dewetting method to fabricate single crystalline faceted Cu nanoparticles attached to a basal plane-oriented sapphire substrate. The annealing conditions were optimized to maximize the formation of equilibrated particles exhibiting the ECS. The Cu-sapphire interface energy determined with the aid of AFM measurement was found to be 1.82 ± 0.15 J m⁻². Only particles with shapes close to the ECS were selected for micro-compression tests, thus minimizing the effect of shape on the particle strength.
- 2. Severe plastic deformation and the accompanying formation of slip traces on the surface results in a unique surface morphology showing smoothed quasi-periodic nanometer-scale asperities, as shown in Fig. 11(c). This type of surface topography can hardly be achieved by classical fabrication means, making the defect-free nanoparticles studied in this work potential candidates for catalytic applications, as such asperities can exhibit increased catalytic activity.
- 3. The load-displacement curves obtained by in situ micro-compression exhibited an initial elastic region followed by a large displacement burst caused by the nucleation of new dislocations in otherwise pristine defect-free nanoparticles. The engineering compressive stress at the onset of the displacement burst was identified with the particle's compressive strength. The size dependence of the strength followed the "smaller is stronger" trend but exhibited two regions with different power law exponents. For particles smaller than 350 nm in diameter, the size dependence of the strength was in excellent agreement with MD simulations implementing a similar compression of much smaller particles. The strength of the particles larger than 350 nm displayed a stronger size dependence, which is consistent with the higher probability of finding a defect in the particle.
- 4. The MD simulations demonstrate that the first dislocation that triggers the particle deformation can nucleate on the surface, usually near a facet edge or a vertex, or homogeneously in a lattice region under a corner. The first dislocation often causes a dislocation avalanche, which stops when all dislocations are eliminated at the particle surface. The subsequent deformation bursts occur at progressively lower stresses due to the accumulation of damage facilitating the dislocation nucleation. This effect is a manifestation of strain softening in dislocation-free nano-systems. Further accumulation of damage restrains the dislocation glide across the particle, eventually changing the deformation mode from nucleation-controlled to glide-controlled. This transition is accompanied by significant strain hardening.
- 5. An Ashby diagram has been constructed for the size dependence of CRSS of pristine faceted particles of four FCC metals (Cu, Pt, Ni, and Au). The diagram plots the CRSS normalized by the shear modulus versus the size normalized by the magnitude of the Burgers vector. No universality is observed in these coordinates. The Pt particles are the weakest, the Ni and Au particles are the strongest, and the Cu particles are in between. This lack of universality in nanoparticle strength was discussed in terms of the non-linearity of the elastic shear moduli under high compressive stresses.
- 6. The mass particle compression method was employed to simultaneously deform a large number of Cu nanoparticles. Most particles exhibited the [111]→[110] re-orientation, while some transformed into polycrystals with co-existing grains with the [110] and

[112] out-of-plane orientations separated by twin boundaries. The former mode of particle reorientation resembles that observed in bulk single crystals of FCC metals. In contrast, the latter mode is unique to the nucleation-controlled small-scale plasticity of metallic nanoparticles. The MD simulations have provided detailed insights into the lattice reorientation mechanism under severe compression.

Acknowledgements

This work was supported by the Israel Science Foundation, grant No. 617/19. Y. M. acknowledges support from the National Science Foundation under Award No. DMR-2103431.

Conflicts of interests

The authors declare that they have no conflicts of interest.

References

- [1] J.R. Greer, J.T.M. De Hosson, Plasticity in small-sized metallic systems: Intrinsic versus extrinsic size effect, Prog. Mater. Sci. 56 (2011) 654–724. https://doi.org/10.1016/j.pmatsci.2011.01.005.
- [2] M.D. Uchic, D.M. Dimiduk, J.N. Florando, W.D. Nix, Sample dimensions influence strength and crystal plasticity, Science (80-.). 305 (2004) 986–989. https://doi.org/10.1126/science.1098993.
- [3] J.R. Greer, W.D. Nix, Nanoscale gold pillars strengthened through dislocation starvation, Phys. Rev. B. 73 (2006). https://doi.org/10.1103/physrevb.73.245410.
- [4] C.A. Volkert, E.T. Lilleodden, Size effects in the deformation of sub-micron Au columns, Philos. Mag. 86 (2006) 5567–5579. https://doi.org/10.1080/14786430600567739.
- [5] D. Kiener, W. Grosinger, G. Dehm, R. Pippan, A further step towards an understanding of size-dependent crystal plasticity: In situ tension experiments of miniaturized single-crystal copper samples, Acta Mater. 56 (2008) 580–592. https://doi.org/10.1016/j.actamat.2007.10.015.
- [6] R. Dou, B. Derby, A universal scaling law for the strength of metal micropillars and nanowires, Scr. Mater. 61 (2009) 524–527. https://doi.org/10.1016/j.scriptamat.2009.05.012.
- [7] H. Bei, S. Shim, E.P. George, M.K. Miller, E.G. Herbert, G.M. Pharr, Compressive strengths of molybdenum alloy micro-pillars prepared using a new technique, Scr. Mater. 57 (2007) 397–400. https://doi.org/10.1016/j.scriptamat.2007.05.010.

- [8] G. Richter, K. Hillerich, D.S. Gianola, R. Mönig, O. Kraft, C.A. Volkert, Ultrahigh strength single crystalline nanowhiskers grown by physical vapor deposition, Nano Lett. 9 (2009) 3048–3052. https://doi.org/10.1021/nl9015107.
- [9] L.Y. Chen, M.R. He, J. Shin, G. Richter, D.S. Gianola, Measuring surface dislocation nucleation in defect-scarce nanostructures, Nat. Mater. 14 (2015) 707–713. https://doi.org/10.1038/nmat4288.
- [10] W.M. Mook, C. Niederberger, M. Bechelany, L. Philippe, J. Michler, Compression of freestanding gold nanostructures: From stochastic yield to predictable flow, Nanotechnology. 21 (2010). https://doi.org/10.1088/0957-4484/21/5/055701.
- [11] D. Mordehai, S.W. Lee, B. Backes, D.J. Srolovitz, W.D. Nix, E. Rabkin, Size effect in compression of single-crystal gold microparticles, Acta Mater. 59 (2011) 5202–5215. https://doi.org/10.1016/j.actamat.2011.04.057.
- [12] A. Sharma, J. Hickman, N. Gazit, E. Rabkin, Y. Mishin, Nickel nanoparticles set a new record of strength, Nat. Commun. 9 (2018). https://doi.org/10.1038/s41467-018-06575-6.
- [13] A. Sharma, R. Kositski, O. Kovalenko, D. Mordehai, E. Rabkin, Giant shape- and size-dependent compressive strength of molybdenum nano- and microparticles, Acta Mater. 198 (2020) 72–84. https://doi.org/10.1016/j.actamat.2020.07.054.
- [14] J. Zimmerman, A. Bisht, Y. Mishin, E. Rabkin, Size and shape effects on the strength of platinum nanoparticles, J. Mater. Sci. 56 (2021) 18300–18312. https://doi.org/10.1007/s10853-021-06435-7.
- [15] I.M. Padilla Espinosa, S. Azadehranjbar, R. Ding, A.J. Baker, T.D.B. Jacobs, A. Martini, Platinum nanoparticle compression: Combining in situ TEM and atomistic modeling, Appl. Phys. Lett. 120 (2022). https://doi.org/10.1063/5.0078035.
- [16] S. Ryu, K. Kang, W. Cai, Entropic effect on the rate of dislocation nucleation, Proc. Natl. Acad. Sci. U. S. A. 108 (2011) 5174–5178. https://doi.org/10.1073/pnas.1017171108.
- [17] Q.J. Li, B. Xu, S. Hara, J. Li, E. Ma, Sample-size-dependent surface dislocation nucleation in nanoscale crystals, Acta Mater. 145 (2018) 19–29. https://doi.org/10.1016/j.actamat.2017.11.048.
- [18] E. Rabkin, D.J. Srolovitz, Onset of plasticity in gold nanopillar compression, Nano Lett. 7 (2007) 101–107. https://doi.org/10.1021/nl0622350.
- [19] A. Cao, E. Ma, Sample shape and temperature strongly influence the yield strength of metallic nanopillars, Acta Mater. 56 (2008) 4816–4828. https://doi.org/10.1016/j.actamat.2008.05.044.
- [20] T.J. Flanagan, O. Kovalenko, E. Rabkin, S.W. Lee, The effect of defects on strength of gold microparticles, Scr. Mater. 171 (2019) 83–86. https://doi.org/10.1016/j.scriptamat.2019.06.023.
- [21] Y. Feruz, D. Mordehai, Towards a universal size-dependent strength of face-centered

- cubic nanoparticles, Acta Mater. 103 (2016) 433–441. https://doi.org/10.1016/j.actamat.2015.10.027.
- [22] C.A. Schuh, J.K. Mason, A.C. Lund, Quantitative insight into dislocation nucleation from high-temperature nanoindentation experiments, Nat. Mater. 4 (2005) 617–621. https://doi.org/10.1038/nmat1429.
- [23] D. Mordehai, O. David, R. Kositski, Nucleation-Controlled Plasticity of Metallic Nanowires and Nanoparticles, Adv. Mater. 30 (2018) 1–17. https://doi.org/10.1002/adma.201706710.
- [24] A. Bisht, R.K. Koju, Y. Qi, J. Hickman, Y. Mishin, E. Rabkin, The impact of alloying on defect-free nanoparticles exhibiting softer but tougher behavior, Nat. Commun. 12 (2021) 2515. https://doi.org/10.1038/s41467-021-22707-x.
- [25] R. Li, S. Lu, D. Kim, S. Schönecker, J. Zhao, S.K. Kwon, L. Vitos, Stacking fault energy of face-centered cubic metals: Thermodynamic and ab initio approaches, J. Phys. Condens. Matter. 28 (2016). https://doi.org/10.1088/0953-8984/28/39/395001.
- [26] D. Chatain, V. Ghetta, P. Wynblatt, Equilibrium Shape of Copper Crystals Grown on Sapphire, Interface Sci. 12 (2004) 7–18. https://doi.org/10.1023/B:INTS.0000012290.07441.a8.
- [27] J. Zimmerman, E. Rabkin, Sculpturing metal nanoparticles by controlled massive deformation, Scripta Mater., in revisio (2024).
- [28] Y. Mishin, M.J. Mehl, D.A. Papaconstantopoulos, A.F. Voter, J.D. Kress, Structural stability and lattice defects in copper: Ab initio, tight-binding, and embedded-atom calculations, Phys. Rev. B Condens. Matter Mater. Phys. 63 (2001) 2241061–22410616. https://doi.org/10.1103/PhysRevB.63.224106.
- [29] S. Plimpton, Fast Parallel Algorithms for Short-Range Molecular Dynamics for the United States Department of Energy under Contract DE.ACO4-76DPOO789, J. Comput. Phys. 117 (1995) 1–19.
- [30] A. Stukowski, Visualization and analysis of atomistic simulation data with OVITO-the Open Visualization Tool, Model. Simul. Mater. Sci. Eng. 18 (2010). https://doi.org/10.1088/0965-0393/18/1/015012.
- [31] J.F. Panzarino, T.J. Rupert, Tracking microstructure of crystalline materials: A post-processing algorithm for atomistic simulations, JOM. 66 (2014) 417–428. https://doi.org/10.1007/s11837-013-0831-9.
- [32] W.L. Winterbottom, Equilibrium shape of a small particle in contact with a foreign substrate, Acta Metall. 15 (1967) 303–310. https://doi.org/10.1016/0001-6160(67)90206-4.
- [33] S. Curiotto, H. Chien, H. Meltzman, P. Wynblatt, G.S. Rohrer, W.D. Kaplan, D. Chatain, Orientation relationships of copper crystals on c-plane sapphire, Acta Mater. 59 (2011) 5320–5331. https://doi.org/10.1016/j.actamat.2011.05.008.
- [34] W.-Z. Han, L. Huang, S. Ogata, H. Kimizuka, Z.-C. Yang, C. Weinberger, Q.-J. Li, B.-

- Y. Liu, X.-X. Zhang, J. Li, E. Ma, Z.-W. Shan, From "Smaller is Stronger" to "Size-Independent Strength Plateau": Towards Measuring the Ideal Strength of Iron, Adv. Mater. 27 (2015) 3385–3390. https://doi.org/10.1002/adma.201500377.
- [35] S. Azadehranjbar, R. Ding, I.M. Padilla Espinosa, A. Martini, T.D.B. Jacobs, Size-Dependent Role of Surfaces in the Deformation of Platinum Nanoparticles, ACS Nano. 17 (2023) 8133–8140. https://doi.org/10.1021/acsnano.2c11457.
- [36] Z.W. Shan, R.K. Mishra, S.A. Syed Asif, O.L. Warren, A.M. Minor, Mechanical annealing and source-limited deformation in submicrometre- diameter Nicrystals, Nat. Mater. 7 (2008) 115–119. https://doi.org/10.1038/nmat2085.
- [37] M.I. Richard, S. Labat, M. Dupraz, J. Carnis, L. Gao, M. Texier, N. Li, L. Wu, J.P. Hofmann, M. Levi, S.J. Leake, S. Lazarev, M. Sprung, E.J.M. Hensen, E. Rabkin, O. Thomas, Anomalous Glide Plane in Platinum Nano- and Microcrystals, ACS Nano. 17 (2023) 6113–6120. https://doi.org/10.1021/acsnano.3c01306.
- [38] F. v. Göler, G. Sachs, Zugversuche an Kristallen aus Kupfer und α-Messing, Zeitschrift Für Phys. 55 (1929) 581–620. https://doi.org/10.1007/BF01333777.
- [39] R.W.K.H. P. Paufler, The plastic deformation of metals, J. Mech. Work. Technol. 12 (1986) 388. https://doi.org/10.1016/0378-3804(86)90011-2.
- [40] D. V. Lychagin, E.A. Alfyorova, D. V. Soprunov, Development of Misorientation in FCC Single Crystals under Compression at Different Scales, IOP Conf. Ser. Mater. Sci. Eng. 142 (2016). https://doi.org/10.1088/1757-899X/142/1/012053.
- [41] Y. Estrin, A. Vinogradov, Extreme grain refinement by severe plastic deformation: A wealth of challenging science, Acta Mater. 61 (2013) 782–817. https://doi.org/10.1016/j.actamat.2012.10.038.
- [42] E. Rabkin, H.S. Nam, D.J. Srolovitz, Atomistic simulation of the deformation of gold nanopillars, Acta Mater. 55 (2007) 2085–2099. https://doi.org/10.1016/j.actamat.2006.10.058.
- [43] W.M. Robertsonh, Faceting of copper surfaces at 1000°C, Acta Metall. 12 (1964) 241–253. https://doi.org/10.1016/0001-6160(64)90193-2.
- [44] W.W. Mullins, Theory of linear facet growth during thermal etching, Philos. Mag. 6 (1961) 1313–1341. https://doi.org/10.1080/14786436108241227.
- [45] F.J. Bradshaw, R.H. Brandon, C. Wheeler, The surface selt-diffusion of copper as affected by environment, Acta Metall. 12 (1964) 1057–1063. https://doi.org/10.1016/0001-6160(64)90077-X.

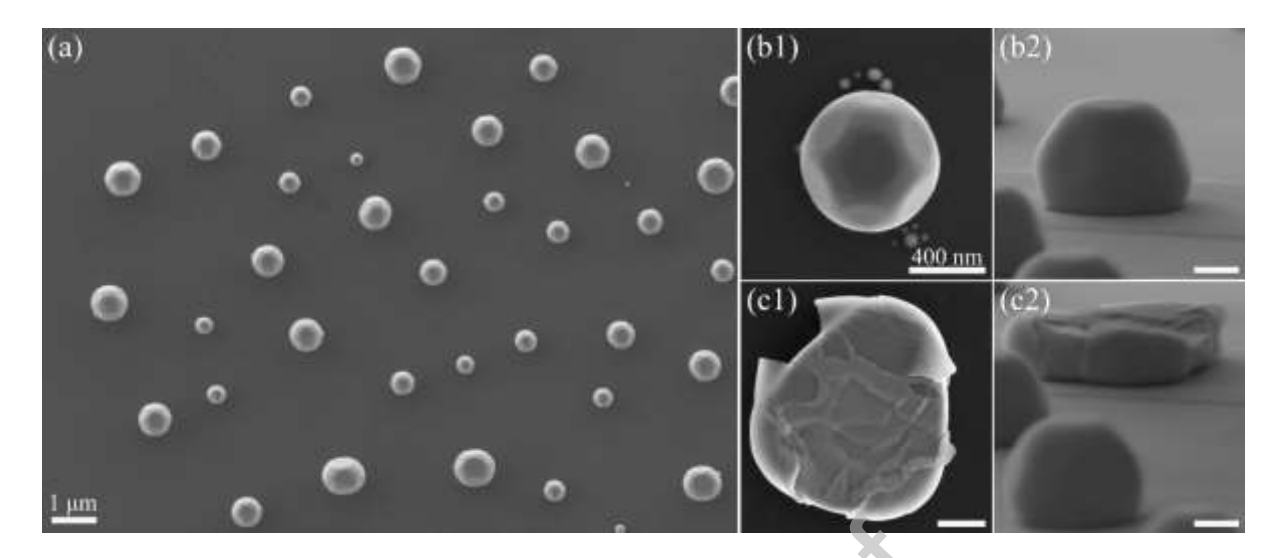


Figure 1: Examples of equilibrated Cu nanoparticles obtained by solid-state dewetting under different conditions. (a) Annealing at 950°C for 48 hours. (b1) plan and (b2) side views (80° tilt) of a particle before indentation. (c1) plane and (c2) side views (80° tilt) of the same particle after indentation. The sample is coated with a thin carbon film to prevent a charging effect during micrograph acquisition.

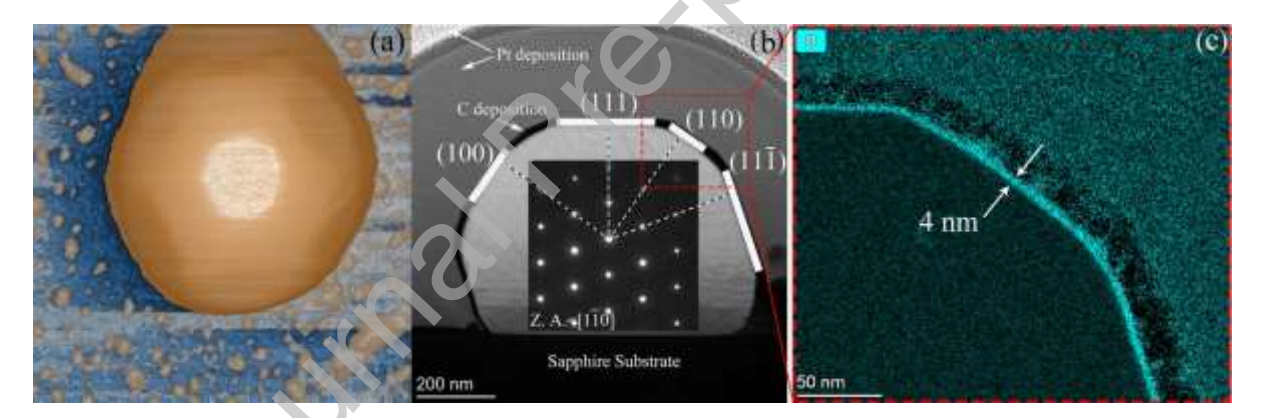


Figure 2: Topography of equilibrated Cu nanoparticle (sample s3). (a) High-resolution AFM topography scan of an equilibrated nanoparticle. (b) Cross-sectional STEM micrograph of an as-dewetted nanoparticle on the sapphire substrate. The diffraction pattern acquired from the upper part of the particle is shown in the inset and confirms that the particle is single crystalline. A narrow twin is visible near the particle bottom. (c) STEM EDS mapping of the near-surface area from (b), showing a thin native oxide layer on the surface.

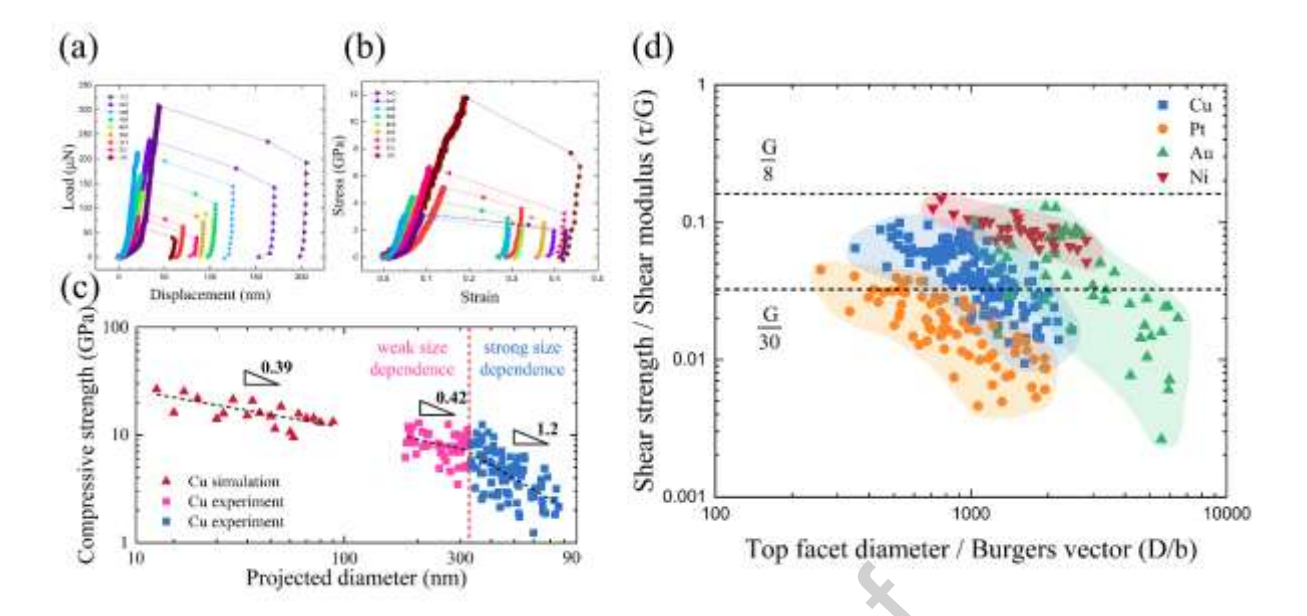


Figure 3: (a) Experimental load-displacement curves for selected Cu particles of various sizes. (b) Engineering stress-strain curves calculated from the load-displacement curves shown in (a). (c) The dependence of the compressive strength of Cu nanoparticles on their projected diameter obtained in MD simulations (particles of up to 100 nm in size) and in the experiment (200-900 nm in size). Two regimes of the size effect on particle strength were indicated in pink and blue colors, separated by the dash vertical line. (d) Comparison of the normalized critical resolved shear stress (CRSS) of Pt, Cu, Ni and Au nanoparticles with dashed lines at G/30 and G/8 representing the lower and upper limits of the theoretical shear strength.

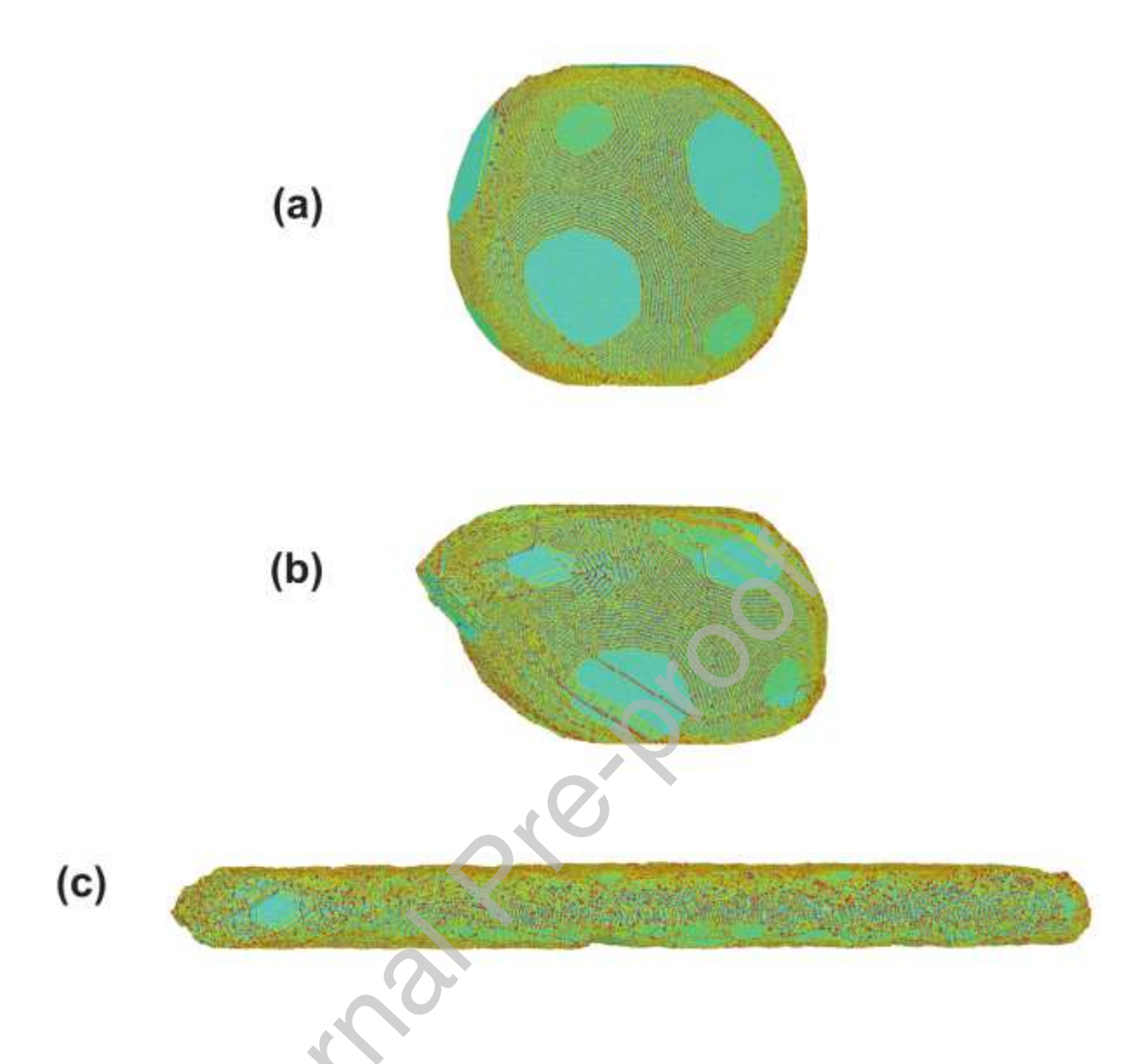


Figure 4: Typical Cu nanoparticle shapes at different stages of simulated compression tests. The atoms are colored by potential energy. (a) Soon after the first peak of stress (strain 0.04). (b) Later stage of compression (strain 0.29). Notice the dislocation slip traces on the surface. (c) Heavily deformed shape (strain 0.76). The initial particle diameter was 40 nm.

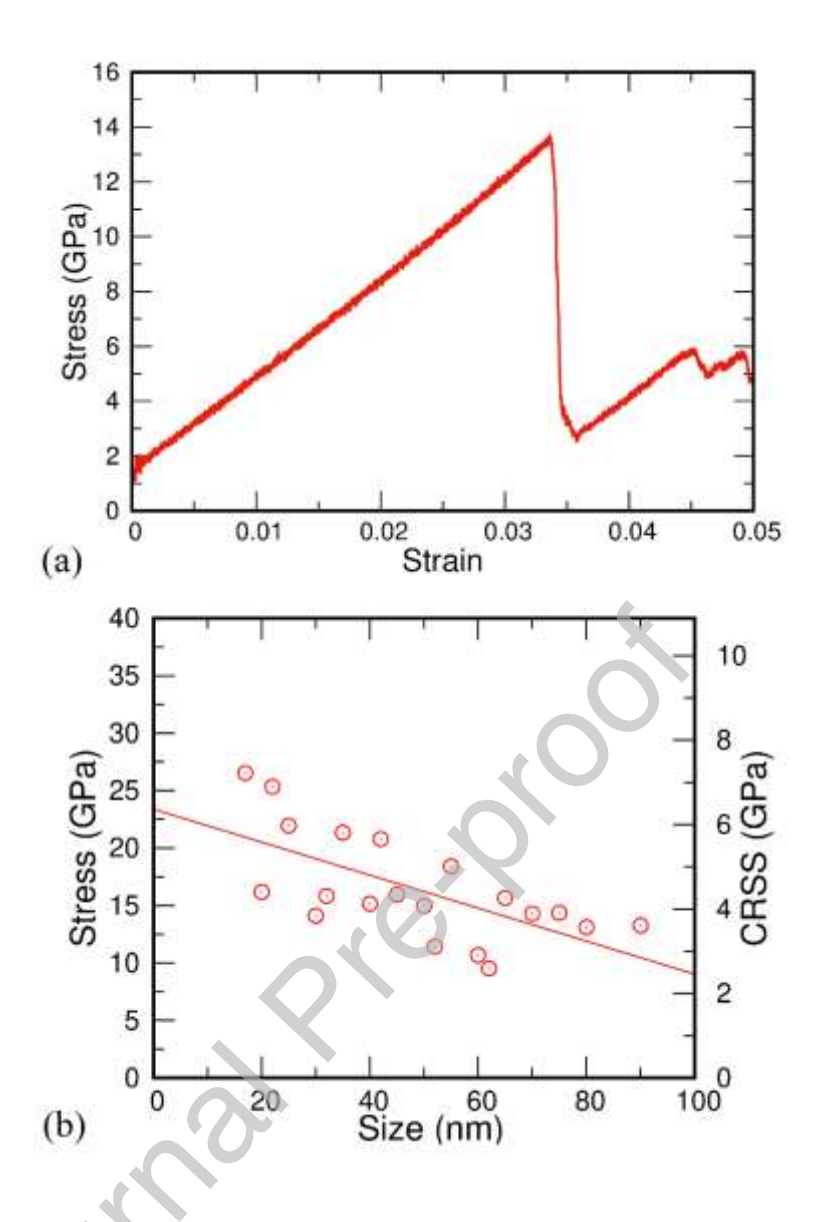


Figure 5: Mechanical strength of Cu nanoparticles from MD simulations. (a) Representative engineering stress-strain curve for a 40 nm nanoparticle showing the first peak of compressive stress. (b) Strength and CRSS as a function of particle size. The solid line represents the linear regression.

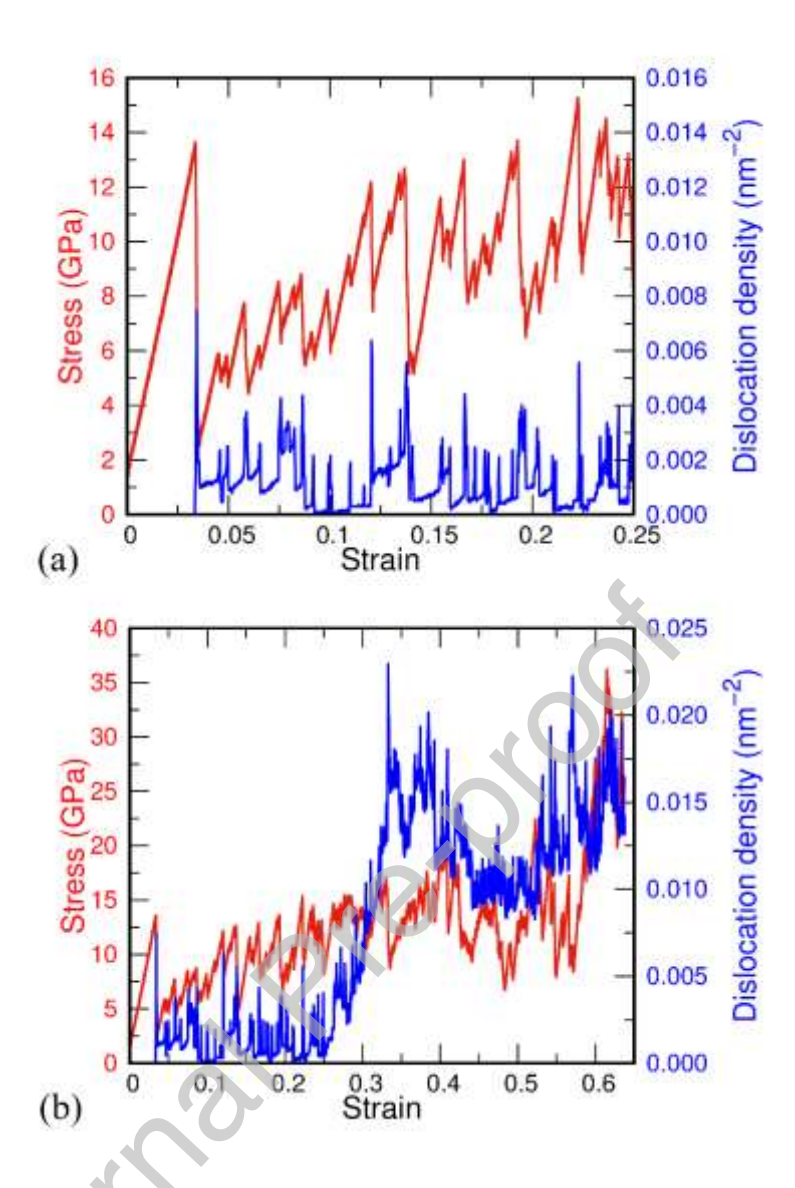


Figure 6: Stress-strain curves demonstrating the strain softening effect followed by strain hardening during nanoparticle compression. (a) Deformation up to the strain of 0.25 showing the strain softening trend. (b) Deformation up to the strain of 0.65 showing accelerated strain hardening under strong compression. The dislocation density plots are shown in blue. The initial diameter of the particle was 40 nm.

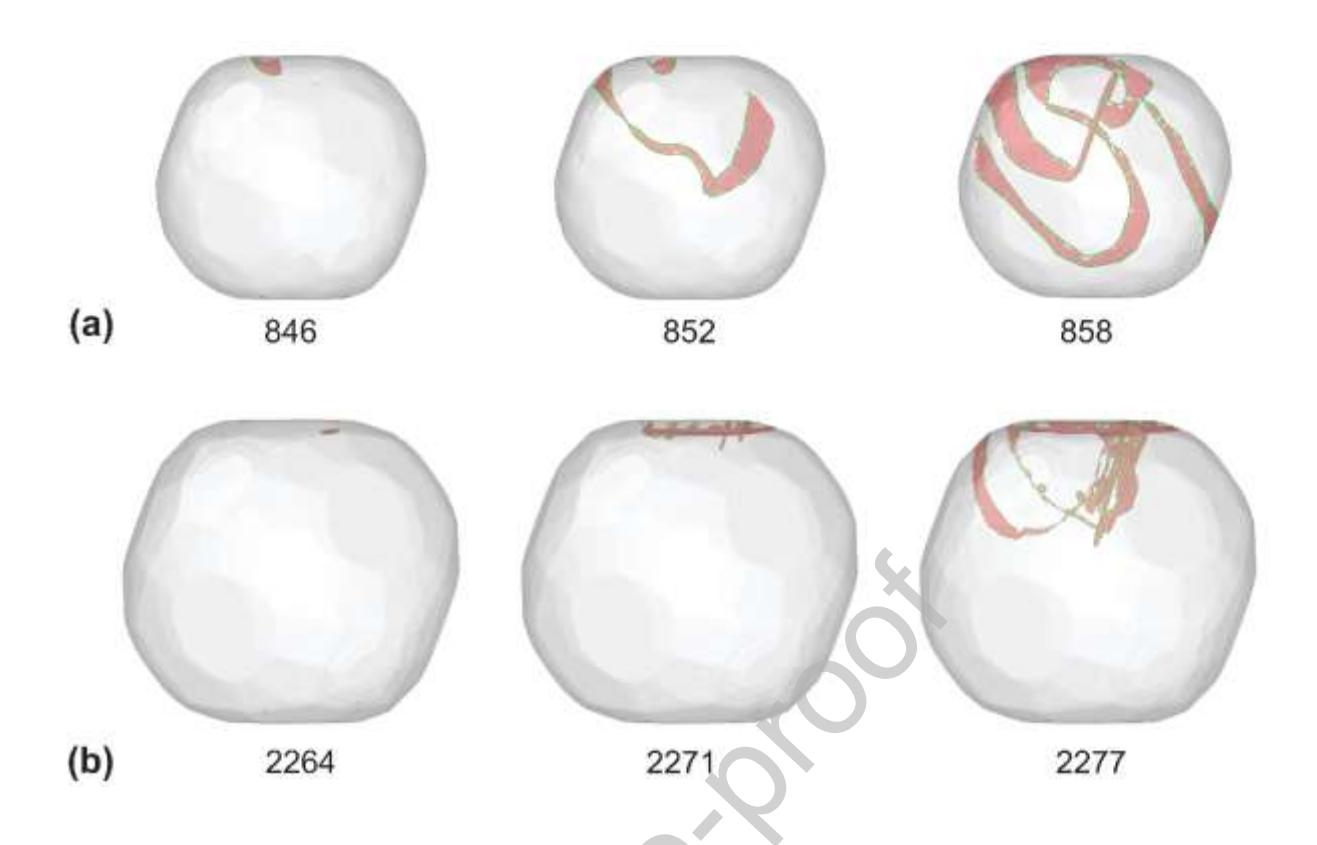


Figure 7: Dislocation mechanisms of plastic deformation in Cu nanoparticles. (a) Surface dislocation nucleation in a 20 nm nanoparticle. (b) Homogeneous dislocation nucleation in a 50 nm nanoparticle. The red atoms decorate intrinsic stacking faults, and the green lines represent Shockley partial dislocations. Atoms in perfect FCC environments are invisible. The numbers indicate the time (in picoseconds) from the start of the simulation.

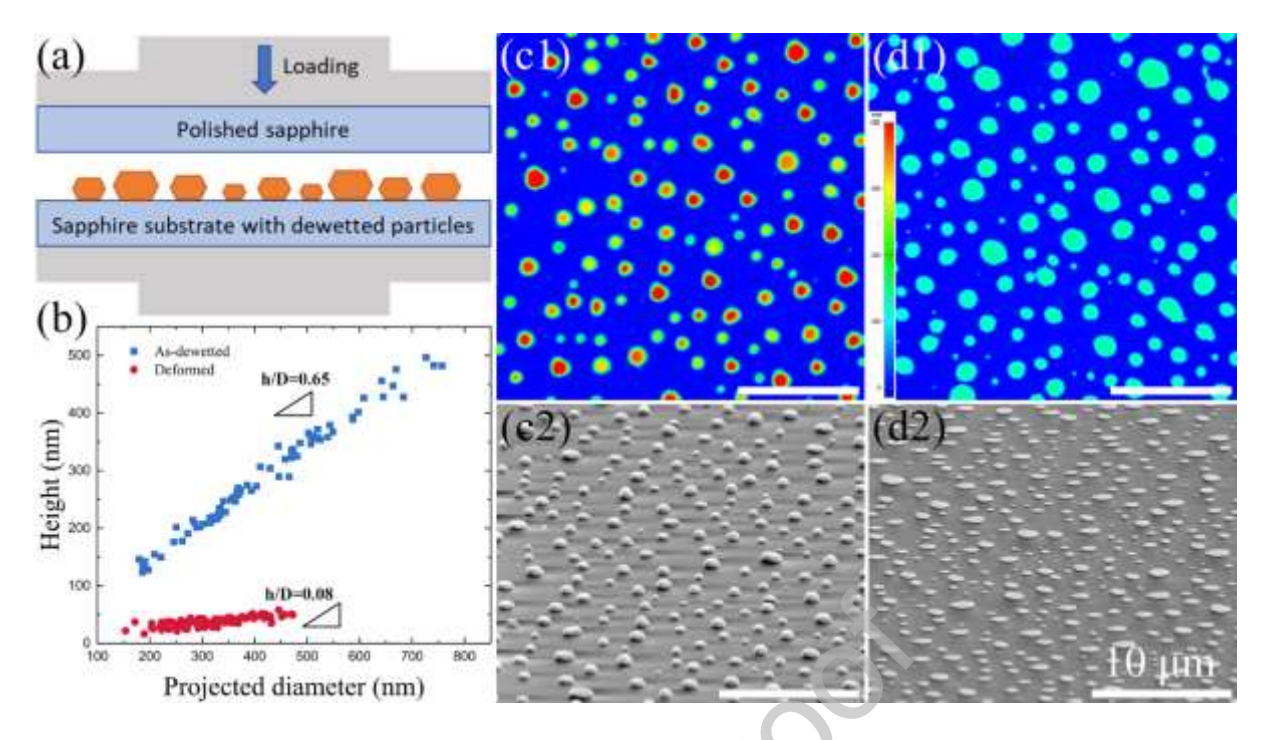


Figure 8: (a) Schematic of the mass particle compression method. (b) Correlation between the height h and projected diameter D of as-dewetted and deformed Cu nanoparticles. (c1) and (d1) AFM topography images of Cu nanoparticles before and after compression, respectively. (c2) and (d2) Secondary electron SEM micrographs of Cu nanoparticles before and after compression, respectively (70° tilted view).

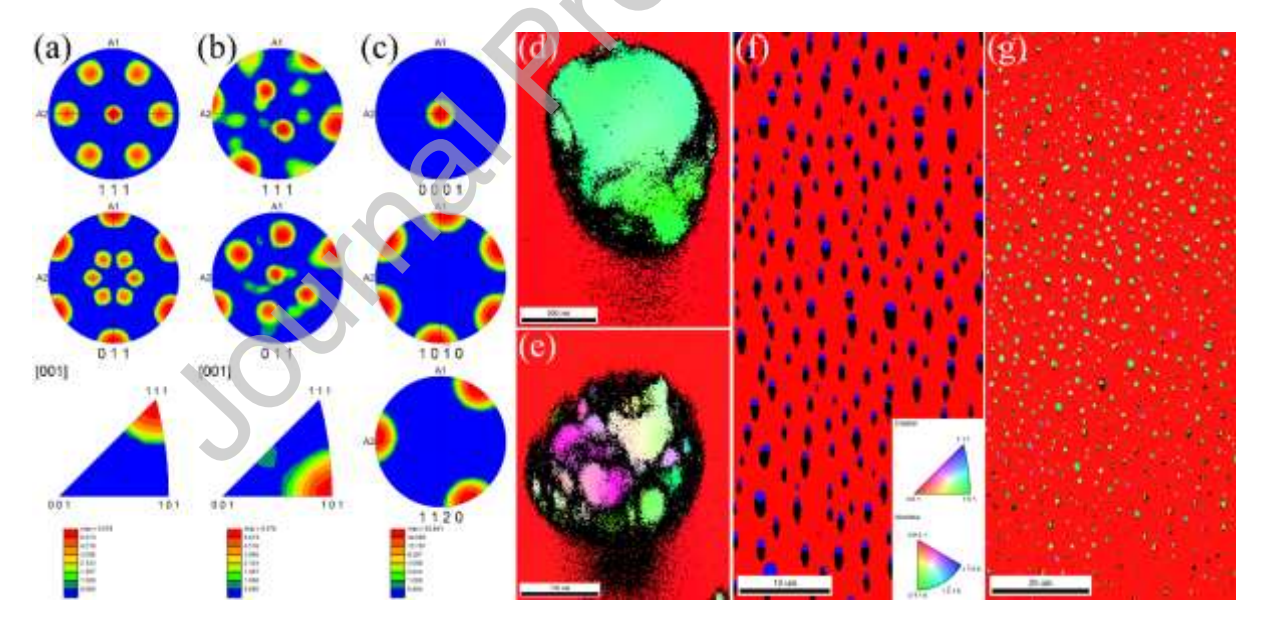


Figure 9: (a), (b), and (c) are pole figures and inverse pole figures of as-dewetted and deformed Cu nanoparticles and of the sapphire substrate derived from EBSD maps in (f) and (g). All pole figures are aligned with (0001) out-of-plane orientation of the substrate as the center point. (a) and (b), from top to bottom: (111) and (110) pole figures and the corresponding inverse pole figures of as-dewetted (a) and deformed (b) Cu nanoparticles. (c) (0001), (1010) and (1120) pole figures (from top to bottom) of the substrate. (d) and (e) are EBSD mappings of two severely deformed particles. The particle in (d) is a single crystal with sub-grains and average [110] out-of-plane orientation. The particle in (e) contains multiple grains separated by high-

angle grain boundaries. (f) and (g) are EBSD mappings of the normal direction of (f) asdewetted and (g) deformed Cu nanoparticles. The color coding of the particle and substrate orientations is shown in the inset in (f).

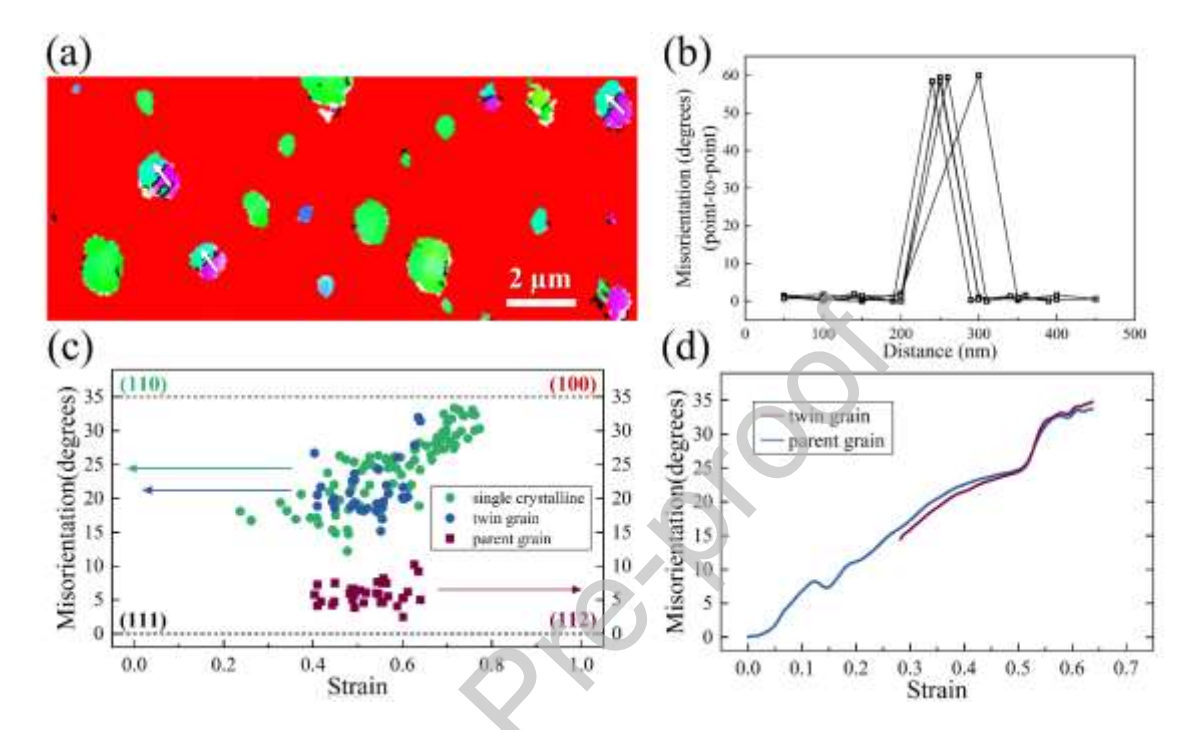


Figure 10: (a) EBSD map of normal directions of a selected group of deformed particles (the color coding is the same as in Fig. 5(f)). (b) Misorientation line profile of five individual deformed particles (category 2) with point-to-point analysis from the parent grain to the nucleated twin grain, indicated by the white arrows in Fig. 6(a). (c) Experimental data on misorientation of two groups of particles deformed to different strains. The misorientation refers to the angular deviation from (111) to (110), and from (112) to (100) for single crystalline deformed particles of category 1 (green dots), and for bicrystalline particles of category 2 with twin grain (blue dots) and parent grain (red squares). (d) Simulation results showing the strain dependence of the misorientation of the parent and twinned grains.

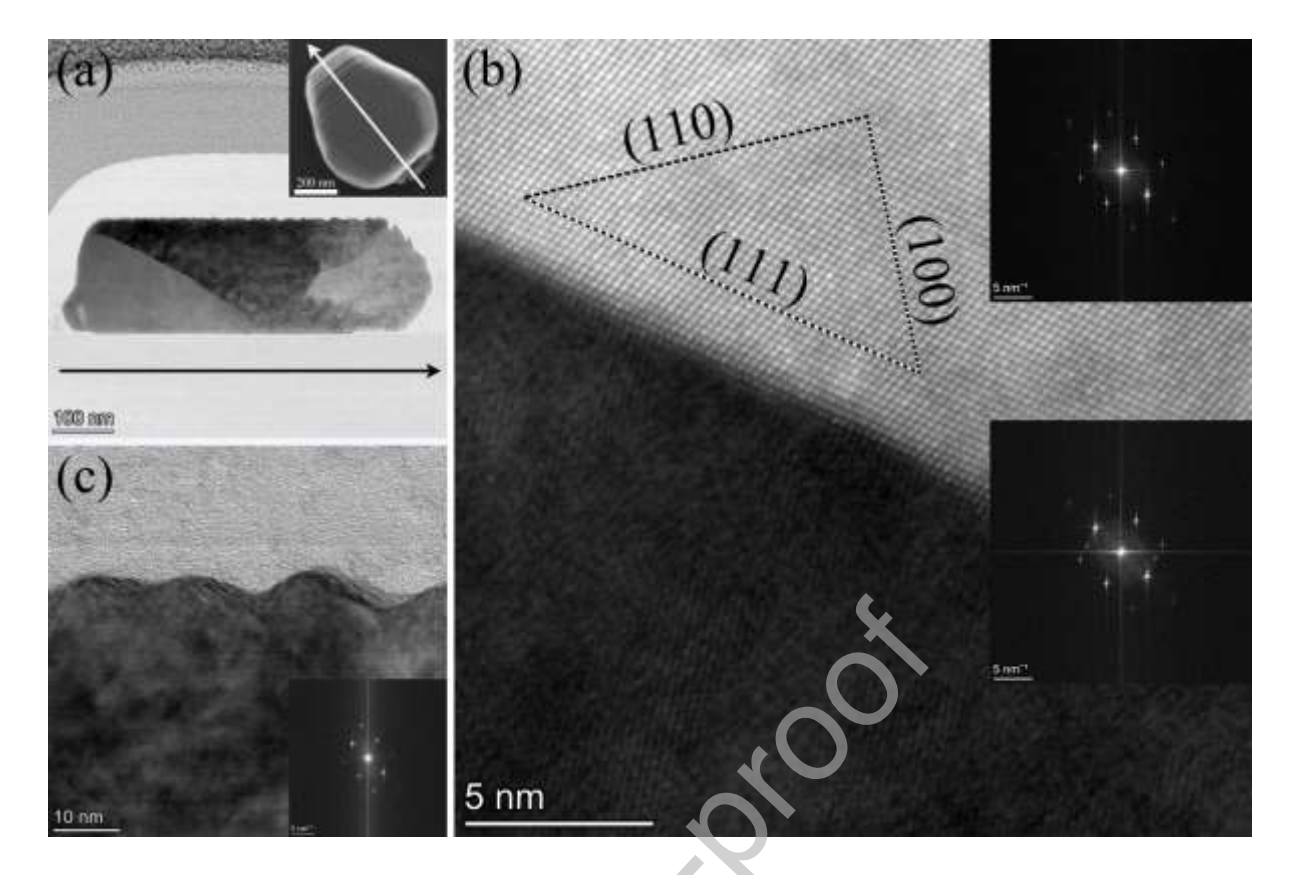


Figure 11: (a) Annular dark filed (ADF) cross-sectional micrograph of a deformed nanoparticle viewed along $[1\bar{1}0]$ direction. The inset is the top view SEM micrograph. (b) High-resolution STEM micrograph of grain boundary between the two largest grains. The upper inset shows the Fast Fourier Transform (FFT) from the upper grain. The lower FFT comes from both grains at the grain boundary. (c) Bright field (BF) micrograph of slip traces on the top surface of the deformed nanoparticle.

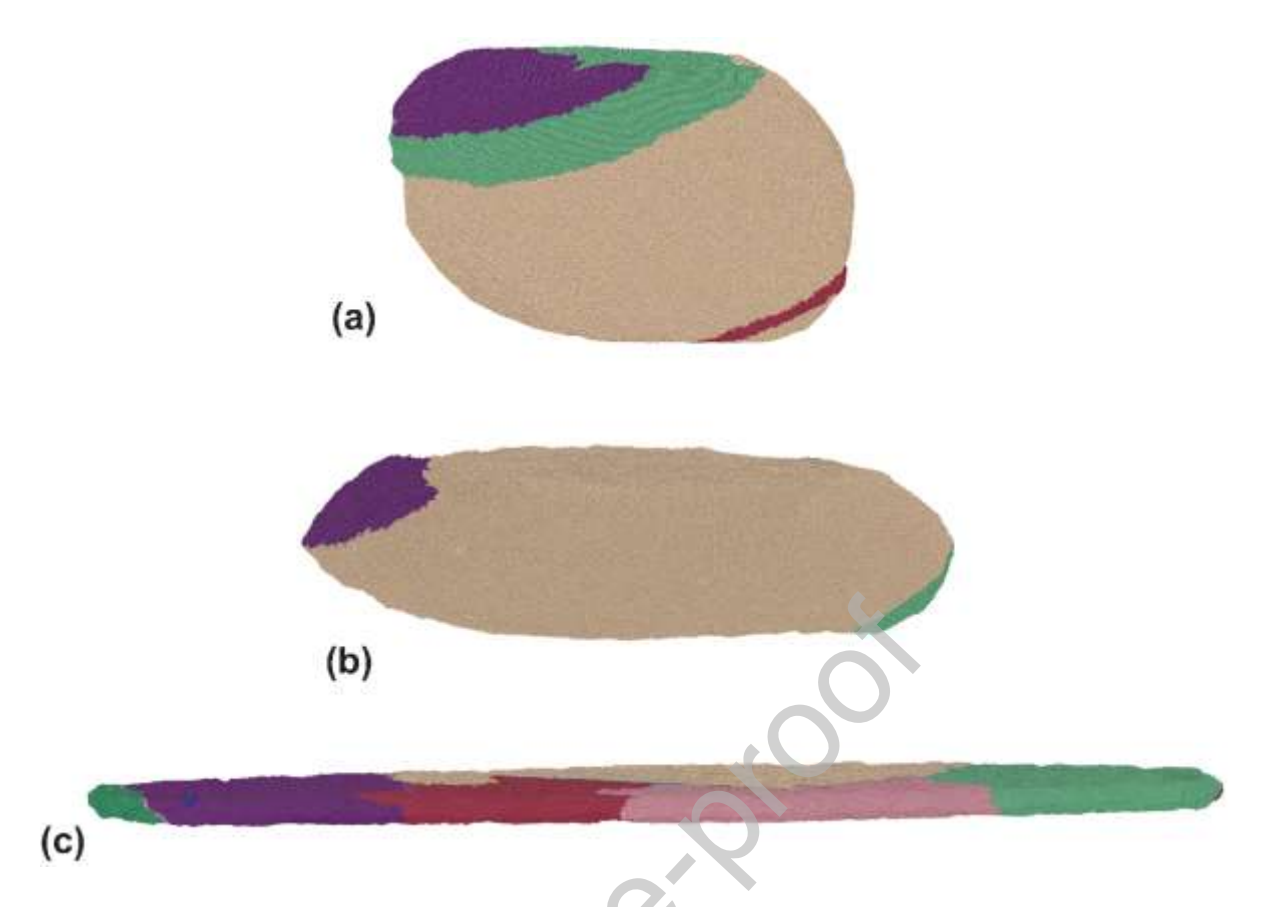


Figure 12: Grain formation in Cu nanoparticles under strong compression (a) Early stage of deformation (strain 0.28) with new grain formation by twining. (b) Stronger deformation (strain 0.58) with new grains nucleated at the periphery. (c) High compression (strain 0.87) causes the formation of more grains. The initial particle diameter was 40 nm. The colors represent different grains.

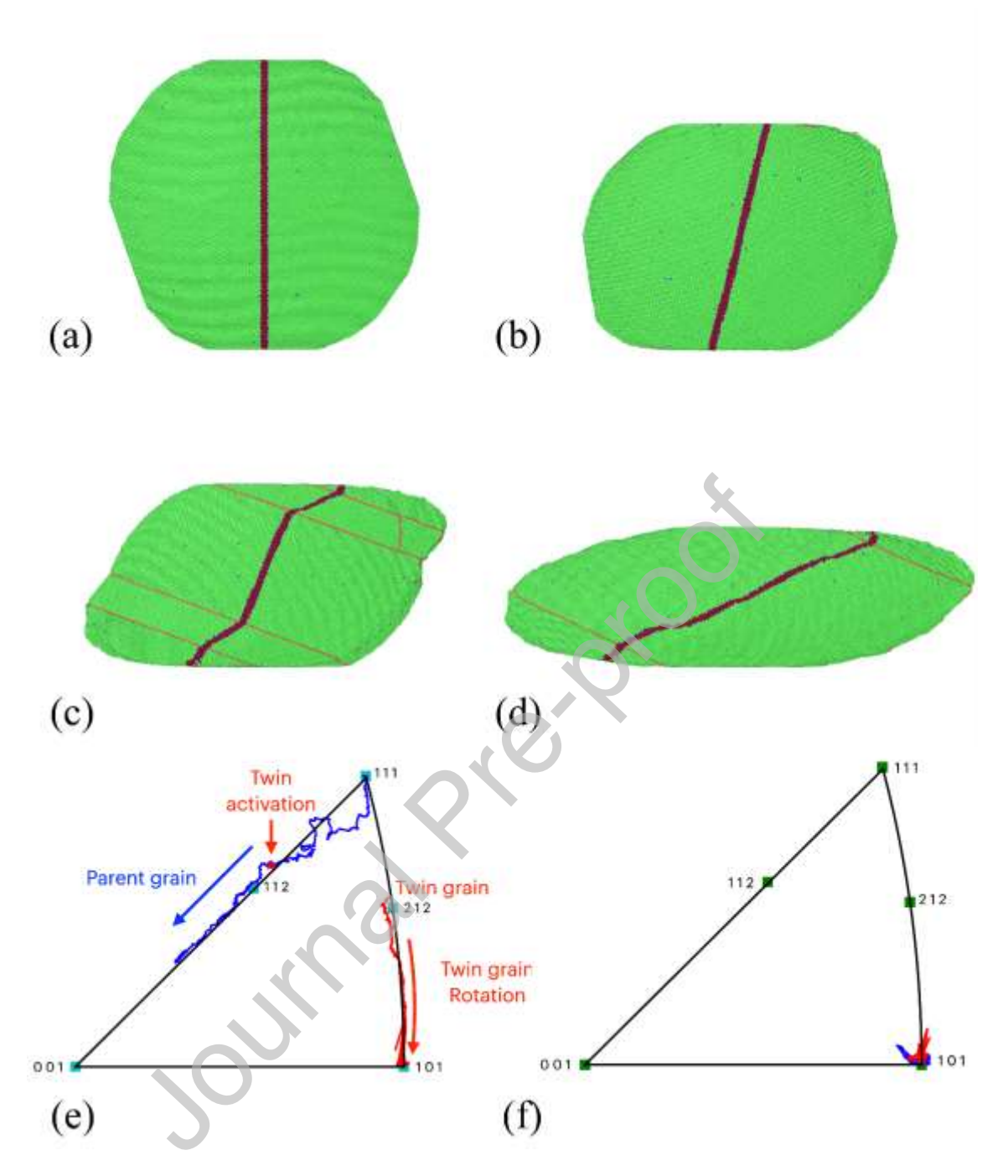


Figure 13: (a)-(d) Shape evolution of a 40 nm nanoparticle. The [110] direction is normal to the page, and the red lines represent twin boundaries. (a) A thin vertical stripe normal to the substrate is chosen as a fiduciary plane to track the lattice rotation. (b) The lattice rotates toward the out-of-plane [100] direction. (c) Twins with the out-of-plane [112] orientation nucleate at the top right and bottom left corners of the particle and grow into the parent grain while their lattice rotates towards [110]. (d) The twins have consumed most of the parent grain and their [110] axis is nearly normal to the substrate. (e) (111) inverse pole figure. (f) (101) inverse pole figure. The blue and red curves show the trajectories of the parent and twin grains, respectively. Note that there is no rotation in the [110] direction normal to the page.

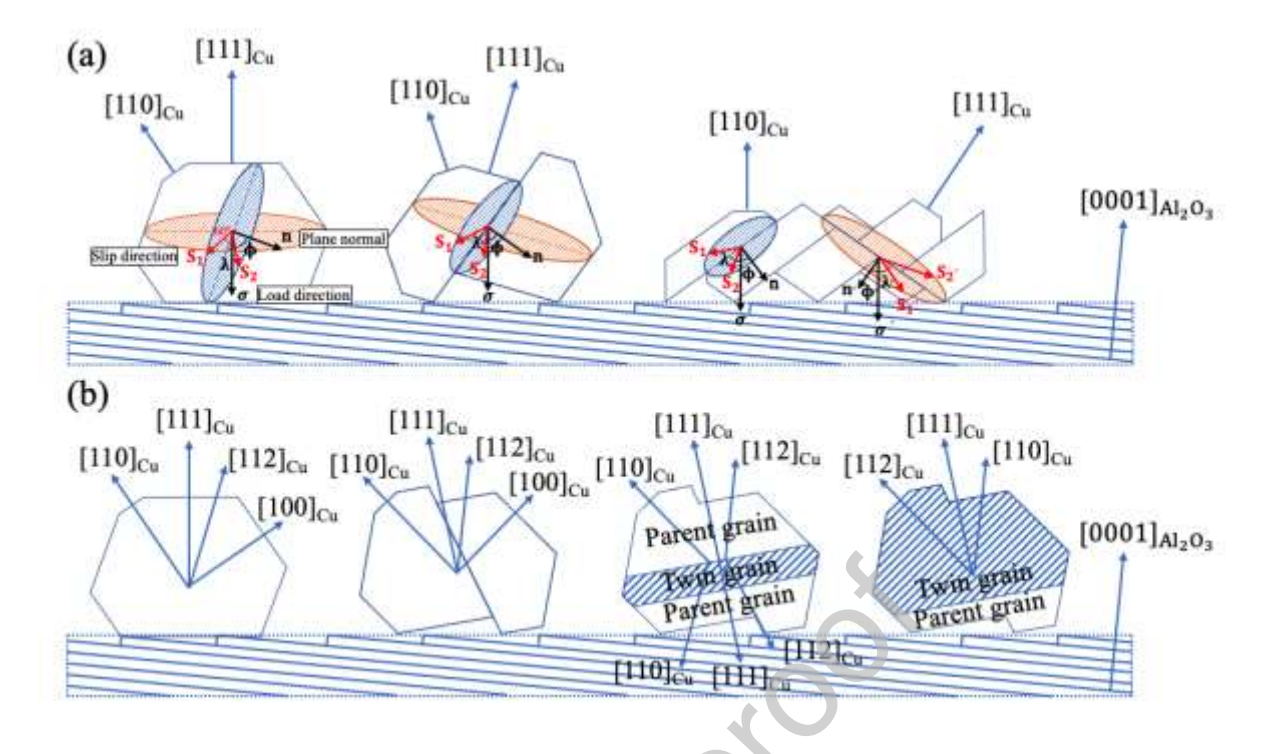
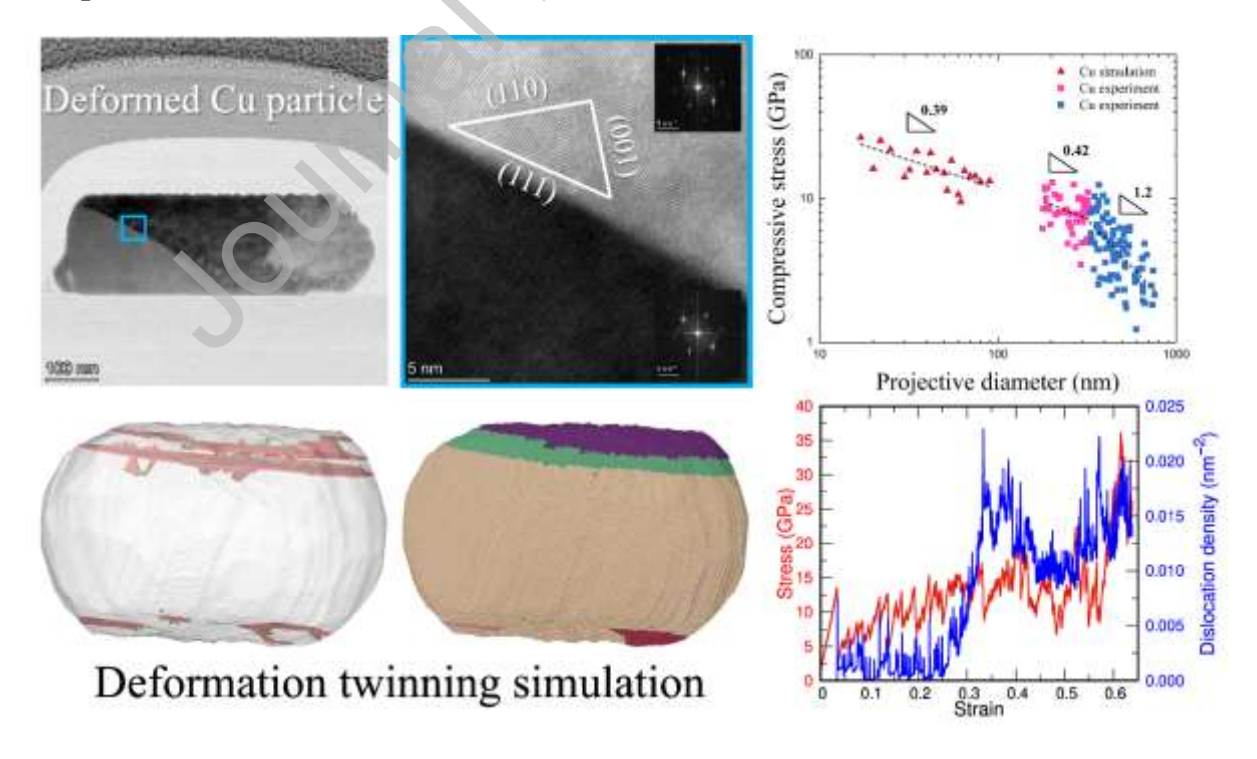


Figure 14: Schematic of two mechanisms of compression-induced nanoparticle rotation on sapphire substrate exhibiting a small mis-cut angle from the basal plane orientation. (a) slip on a single {111} plane; (b) slip on two {111} planes followed by nucleation of a twinned grain and its expansion.

Graphical Abstract



Declaration of interests

•	o known competing financial interests or personal to influence the work reported in this paper.
□The authors declare the following fina considered as potential competing interes	ncial interests/personal relationships which may be ests: